

# Inverse $\text{In}_2\text{O}_{3-x}/\text{Ni}$ interfaces via $\text{Ni}_3\text{InC}_{0.5}$ surface reconstruction for efficient $\text{CO}_2$ hydrogenation to methanol

Received: 15 February 2025

Accepted: 27 October 2025

Published online: 08 December 2025

Check for updates

Jiyi Chen<sup>1,2,3,8</sup>, Tiantian Xiao<sup>1,3,8</sup>, Bingqing Yao<sup>4,8</sup>, Maoshuai Li<sup>1,3</sup>✉, Heng Zhang<sup>1</sup>, Mingwu Tan<sup>5</sup>, Shibo Xi<sup>5</sup>, Shixiong Tang<sup>1</sup>, Wenyan Jia<sup>1,2,3</sup>, Qi Yang<sup>1</sup>, Ziwen Hao<sup>1,2,3</sup>, Zhenmei Zhang<sup>1,2,3</sup>, Kang Hui Lim<sup>2</sup>, Xiaoyu Han<sup>1</sup>, Xiaohui Zi<sup>1</sup>, Yue Wang<sup>1</sup>, Jing Lv<sup>1</sup>, Qian He<sup>4</sup>, Yong Wang<sup>1</sup>✉, Sibudjing Kawi<sup>2</sup>✉ & Xinbin Ma<sup>1,6,7</sup>✉

Catalyst surface reconstruction under reaction conditions is ubiquitous and crucial for creating unusual active sites, thereby enhancing catalytic performance. Here, we report the surface reconstruction of supported  $\text{Ni}_3\text{InC}_{0.5}$  nanoparticles, leading to the formation of defective  $\text{In}_2\text{O}_{3-x}$  overlayers and inverse  $\text{In}_2\text{O}_{3-x}/\text{Ni}$  interfaces, driven by  $\text{CO}_2$ -induced selective surface oxidation during  $\text{CO}_2$  hydrogenation. The synergy between  $\text{In}_2\text{O}_{3-x}$  overlayers and inverse  $\text{In}_2\text{O}_{3-x}/\text{Ni}$  interfaces facilitates  $\text{CO}_2$  adsorption and activation, as well as the following hydrogenation of  $\text{HCOO}^+$  and  $\text{CH}_x\text{O}^+$  intermediates, enabling efficient methanol synthesis from  $\text{CO}_2$ . Accordingly, the optimized LDH- $\text{NiInCAl}$  catalyst achieves an impressive  $\text{CO}_2$  conversion of 19% with 65% methanol selectivity and  $508.4 \text{ mg}_{\text{cat}}^{-1} \text{ h}^{-1}$  methanol space-time yield at  $260^\circ\text{C}$ , 5 MPa, and  $12000 \text{ mL}_{\text{cat}}^{-1} \text{ h}^{-1}$ , outperforming commercial  $\text{Cu}/\text{ZnO}/\text{Al}_2\text{O}_3$  catalysts. This work showcases how structural evolution and surface reconstruction enhance catalytic performance, providing new insights into the dynamic structure-activity relationship.

Surface reconstruction of catalysts, triggered by structural evolution during pretreatments or reactions, can give rise to new surface structures distinct from their original state<sup>1</sup>. This phenomenon is prevalent in redox reactions—such as  $\text{CO}_2$  hydrogenation<sup>2–5</sup>, CO oxidation<sup>6</sup>, Fischer-Tropsch synthesis<sup>7</sup>, and methane dry reforming<sup>8,9</sup>, where the dynamic redox environment facilitates these transformations. Diverse structural changes can enhance or modify catalytic activity and selectivity<sup>2–6</sup>, and in some cases

improve stability<sup>8,10</sup>. Despite the recognized importance of catalyst structural evolution and surface reconstruction, their precise characterization remains challenging due to the demands of high-resolution and in-situ techniques<sup>11,12</sup>. These constraints hinder accurate understandings of the structure-performance relationship and the underlying mechanisms driving catalytic behavior, thereby limiting the effective utilization of surface reconstruction in catalyst design.

<sup>1</sup>Key Laboratory for Green Chemical Technology of Ministry of Education, Collaborative Innovation Center of Chemical Science and Engineering, School of Chemical Engineering and Technology, Tianjin University, Tianjin, China. <sup>2</sup>Department of Chemical and Biomolecular Engineering, College of Design and Engineering, National University of Singapore, Singapore, Singapore. <sup>3</sup>Joint School of National University of Singapore and Tianjin University, International Campus of Tianjin University, Fuzhou, China. <sup>4</sup>Department of Materials Science and Engineering, College of Design and Engineering, National University of Singapore, Singapore, Singapore. <sup>5</sup>Institute of Sustainability for Chemicals, Energy and Environment, Agency for Science, Technology and Research (A\*STAR), Singapore, Singapore. <sup>6</sup>Haihe Laboratory of Sustainable Chemical Transformations, Tianjin, China. <sup>7</sup>School of Chemical Engineering and Technology, Xinjiang University, Urumqi, China. <sup>8</sup>These authors contributed equally: Jiyi Chen, Tiantian Xiao, Bingqing Yao. ✉e-mail: [maoshuaili@tju.edu.cn](mailto:maoshuaili@tju.edu.cn); [yong.wang@tju.edu.cn](mailto:yong.wang@tju.edu.cn); [chekawis@nus.edu.sg](mailto:chekawis@nus.edu.sg); [xbma@tju.edu.cn](mailto:xbma@tju.edu.cn)

In the past decade, CO<sub>2</sub> hydrogenation to methanol has garnered significant attention as a promising and sustainable route for chemical and fuel production, supporting the global pursuit of net-zero industrial emissions<sup>13</sup>. Traditionally, Cu/ZnO/Al<sub>2</sub>O<sub>3</sub> (CZA) catalyst has been the benchmark catalyst for industrial methanol synthesis from CO or CO<sub>2</sub>, leveraging the interplay between Cu and ZnO to enhance methanol selectivity through the formation of ZnO<sub>x</sub> species on Zn-decorated Cu or Cu-Zn alloy nanoparticles (NPs) under CO<sub>2</sub>/H<sub>2</sub> atmospheres<sup>14,15</sup>. However, the structural sensitivity to reaction atmospheres leads to ongoing catalyst evolution, including sintering and valence change of Cu species with ZnO agglomeration, which compromises its long-term stability<sup>16</sup>. This trade-off has driven the search for alternative catalysts for CO<sub>2</sub>-to-methanol conversion. Recently, theoretical studies have demonstrated that In<sub>2</sub>O<sub>3</sub> is excellent for CO<sub>2</sub> activation and stabilization of key intermediates in methanol synthesis<sup>17,18</sup>, exhibiting even higher methanol selectivity and activity than conventional Cu-based catalysts<sup>19</sup>. This insight has spurred growing interest in the development of more efficient In<sub>2</sub>O<sub>3</sub>-based catalysts for CO<sub>2</sub>-to-methanol conversion. As a result, significant progress has been made in the design of advanced In<sub>2</sub>O<sub>3</sub>-based catalytic systems, including In<sub>2</sub>O<sub>3</sub>-supported metal catalysts<sup>20,21</sup> and zirconia-supported In<sub>2</sub>O<sub>3</sub> catalysts<sup>22,23</sup>. Typically, introducing metal promoters, such as Pd or Ni compensates for the inherently weak H<sub>2</sub> activation ability of In<sub>2</sub>O<sub>3</sub>, significantly boosting methanol production rates<sup>20,21</sup>. Meanwhile, the formation of In-based intermetallic compounds (IMCs) may provide more active sites for intermediate stabilization<sup>24,25</sup>. However, the ultra-high H<sub>2</sub> activation capability of these metals can inadvertently lead to over-reduction of the In<sub>2</sub>O<sub>3</sub> support. Although such

catalysts often exhibit high initial performance, this over-reduction impairs the CO<sub>2</sub> activation ability of In<sub>2</sub>O<sub>3</sub> and ultimately undermines catalyst stability<sup>26,27</sup>. So far, achieving stable metal/In<sub>2</sub>O<sub>3</sub> interfaces, such as Ni/In<sub>2</sub>O<sub>3</sub>, remains a key but challenging issue in practice.

In this context, we report the surface reconstruction of supported Ni<sub>3</sub>InC<sub>0.5</sub>NPs during CO<sub>2</sub> hydrogenation that can induce stable defective In<sub>2</sub>O<sub>3-x</sub> overlayers on the carbide phase. This unique structure introduces additional active sites for CO<sub>2</sub> adsorption, stabilizes formate intermediates, and establishes robust inverse In<sub>2</sub>O<sub>3-x</sub>/Ni interfaces featured with highly active asymmetric Ni-In sites, enabling accelerated hydrogenation of formate intermediates and methanol production. On this basis, an alumina-supported NiIn carbide catalyst derived from layered double hydroxide (LDH-NiInCAI) was developed, achieving an impressive CO<sub>2</sub> conversion of 19%, methanol selectivity of 65%, and a methanol space-time yield of 508.4 mg<sub>cat</sub><sup>-1</sup> h<sup>-1</sup> at 260 °C, 5 MPa, and 12000 mL<sub>cat</sub><sup>-1</sup> h<sup>-1</sup>. This performance surpasses that of commercial Cu/ZnO/Al<sub>2</sub>O<sub>3</sub> catalysts, ranks among the best state-of-the-art catalysts reported, and demonstrates strong potential for industrial methanol synthesis from CO<sub>2</sub>.

## Results

### Synthesis of supported Ni<sub>3</sub>InC<sub>0.5</sub> catalysts

Figure 1a and Supplementary Fig. 1 illustrates the synthetic approach employed to produce supported Ni<sub>3</sub>InC<sub>0.5</sub> catalysts for efficient and stable CO<sub>2</sub> hydrogenation to methanol, detailing the crystal structural evolution from Ni<sub>3</sub>In to Ni<sub>3</sub>InC<sub>0.5</sub>. In brief, during thermal treatment under a 25 vol% CO<sub>2</sub>/H<sub>2</sub> gas flow at 600 °C, as determined by H<sub>2</sub> temperature-programmed reduction (H<sub>2</sub>-TPR) profiles

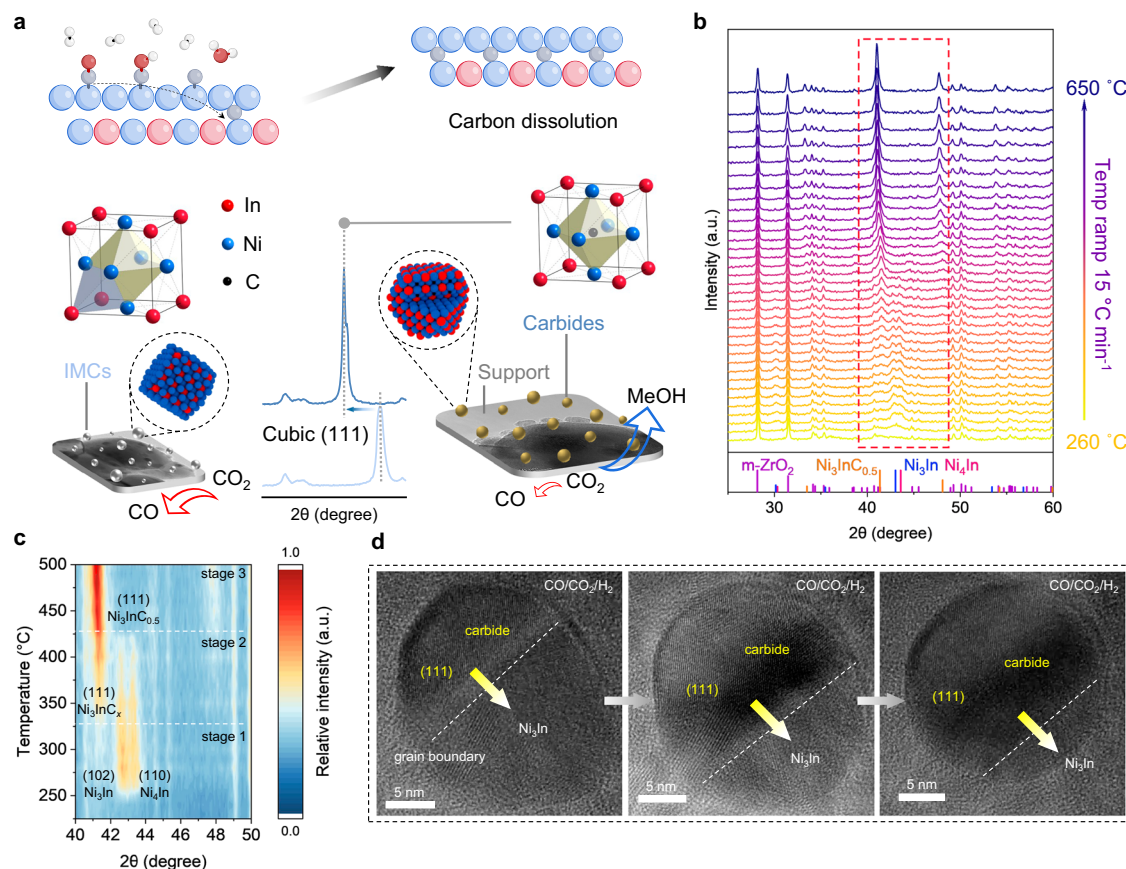


**Fig. 1 | Synthesis of supported Ni<sub>3</sub>InC<sub>0.5</sub> catalysts.** **a** Schematic illustration of the structure and phase transformation of Ni<sub>3</sub>InC<sub>0.5</sub> catalysts. The molecular models represent H<sub>2</sub>, CO, and H<sub>2</sub>O, respectively. **b, c** In-situ XRD patterns (**b**) and contour maps (**c**) of the supported NiIn precursor under 25 vol% CO<sub>2</sub>/H<sub>2</sub> during the heating

process. Numbers in parentheses indicate the representative crystalline planes of the specific species. **d** In-situ HRTEM images of a supported Ni<sub>3</sub>In NP. White dotted lines: grain boundary between Ni<sub>3</sub>InC<sub>0.5</sub> and Ni<sub>3</sub>In. Yellow arrows: direction of the grain boundary moving. Atmosphere: CO/CO<sub>2</sub>/H<sub>2</sub> = 10:22.5:67.5, 400 °C, 1 bar.

(Supplementary Fig. 2), the supported oxide precursor NiInZrO, comprising NiO, In<sub>2</sub>O<sub>3</sub>, and an oxide support (monoclinic zirconia as a paradigm), is initially reduced by H<sub>2</sub> to generate supported Ni<sub>3</sub>In IMC NPs. These supported IMC NPs then facilitate the reverse water-gas shift (RWGS) reaction, producing CO as the carburizing agent<sup>28</sup>. Adsorbed CO subsequently reacts with Ni<sub>3</sub>In NPs, as described by Eq. (1), wherein carbon atoms diffuse into the Ni<sub>3</sub>In lattice and occupy octahedral interstices of Ni<sup>10</sup>, leading to lattice expansion and phase transformation to Ni<sub>3</sub>InC<sub>0.5</sub>.



In addition to the zirconia-supported Ni<sub>3</sub>In and Ni<sub>3</sub>InC<sub>0.5</sub> catalysts, named NiInZr and NiInCZr, we also designed supported Ni<sub>3</sub>Zn, Ni<sub>3</sub>Ga, and their corresponding carbide catalysts as reference samples for explorative and extended studies. X-ray diffraction (XRD) analysis identified the supported species in the two NiIn catalysts as hexagonal Ni<sub>3</sub>In (DO<sub>19</sub>-type IMCs) and cubic Ni<sub>3</sub>InC<sub>0.5</sub> (derived from L1<sub>2</sub>-type IMCs) (Supplementary Fig. 3)<sup>29,30</sup>. X-ray fluorescence spectroscopy (XRF) confirmed that the nominal Ni content (33 wt.%) and Ni/In stoichiometric ratio ( $R_{\text{Ni/In}} = 3.0$ ) in NiInCZr are accurately achieved (Supplementary Table 1). Textural property measurements revealed that both catalysts exhibit similar surface areas and pore volumes (Supplementary Table 2). High-resolution transmission electron microscopy (HRTEM) images showed that both catalysts possess classical supported-catalyst architectures, with IMC/carbide NPs approximately 11 nm in size randomly distributed across the monoclinic ZrO<sub>2</sub> (m-ZrO<sub>2</sub>) support surface (Supplementary Figs. 4–6).

The carbide formation mechanism was elucidated by monitoring the carburization at both macro and micro scales. Specifically, in-situ XRD and in-situ thermogravimetric analysis (TGA) identified three distinct transformation stages for the NiInZrO precursor during carburization (Fig. 1b,c and Supplementary Figs. 7,8): (i) formation of IMCs (Ni<sub>3</sub>In and Ni<sub>4</sub>In), (ii) conversion of IMCs to carbide (Ni<sub>3</sub>InC<sub>x</sub>, where  $x < 0.5$ ), and (iii) further carburization to Ni<sub>3</sub>InC<sub>0.5</sub>, supporting the process of alloying, CO production, then carburization. In-situ HRTEM studies provided nanoscale insights into the evolution mechanism, visualizing the gradual transformation of NPs from Ni<sub>3</sub>In to Ni<sub>3</sub>InC<sub>0.5</sub> during the RWGS reaction (Fig. 1d and Supplementary Movie 1). The movement of the grain boundary between Ni<sub>3</sub>InC<sub>0.5</sub> and Ni<sub>3</sub>In phases demonstrates the phase transformation, progressing from one side of NPs to the other under the CO/CO<sub>2</sub>/H<sub>2</sub> atmosphere. Insights from theoretical calculations suggest that the underlying mechanism might be easier C formation from CO on the carbide surface (Supplementary Fig. 9).

### In<sub>2</sub>O<sub>3-x</sub> overlayers on Ni<sub>3</sub>InC<sub>0.5</sub> NPs via surface reconstruction

Accompanying the phase transformation, a nanoscale overlayer with low crystallinity was observed covering the surface of Ni<sub>3</sub>InC<sub>0.5</sub> (Supplementary Fig. 10), as further verified by the quasi-in-situ aberration-corrected high-angle annular dark-field scanning transmission electron microscopy (AC-HAADF-STEM) analysis of the NiInCZr catalyst transferred under vacuum conditions after carburization (Fig. 2a). The composition and origin of this overlayer were further explored by comparing the X-ray photoelectron spectroscopy (XPS) spectra of the air-passivated and re-activated NiIn carbide catalyst, transferred inertly by a specialist sample holder. Following reactivation of the passivated sample under a 25 vol% CO<sub>2</sub>/H<sub>2</sub> flow at 400 °C and 1 bar, the peaks of oxidative Ni disappeared, while those of indium oxides partially remained (Supplementary Fig. 11). Therefore, overlayers on Ni<sub>3</sub>InC<sub>0.5</sub> NPs are composed of In<sub>2</sub>O<sub>3</sub> derived from surface reconstruction, specifically the selective oxidation of the Ni<sub>3</sub>InC<sub>0.5</sub> phase during the RWGS reaction. AC-HAADF-STEM image of the fresh NiInCZr sample further identified the overlayers, approximately 1 nm thick, as cubic

In<sub>2</sub>O<sub>3</sub> with an exposed (400) facet (lattice spacing of 2.53 Å) (Fig. 2b and Supplementary Fig. 12).

Notably, this selective surface oxidation occurs exclusively on the Ni<sub>3</sub>InC<sub>0.5</sub> phase, as no changes, neither carburization nor surface oxidation, were observed over the Ni<sub>3</sub>In phase during the in-situ STEM experiment under the CO<sub>2</sub>/H<sub>2</sub> atmosphere without CO co-feeding (Fig. 2c and Supplementary Fig. 13).

More solid evidence of surface reconstruction was obtained through multiple in-situ spectroscopic characterizations, as detailed in Supplementary Table 3 and the Methods section. For in-situ Raman spectroscopy, an unsupported Ni<sub>3</sub>InC<sub>0.5</sub> (NiInC) sample was carburized using pure CO in advance to remove the air-passivated oxide layer and avoid interference from the Raman peaks of the ZrO<sub>2</sub> support (Supplementary Fig. 14). Upon introducing 25 vol% CO<sub>2</sub>/H<sub>2</sub> gas into the in-situ cell, two new bands at 106 and 305 cm<sup>-1</sup> appeared and gradually intensified, corresponding to In-O vibration and δ bending vibration ( $E_{1g}$ ) modes in the [InO<sub>6</sub>] octahedral units of c-In<sub>2</sub>O<sub>3</sub>, respectively (Fig. 2d)<sup>31–33</sup>. Importantly, no peaks assigned to NiO species were detected<sup>34</sup>, reinforcing the selective feature of surface oxidation.

In-situ XPS also substantiated these findings (Fig. 2e and Supplementary Table 4). In the Ni 2*p* spectra, peaks at binding energy (BE) of 852.4, 855.6, and 861.4 eV correspond to Ni<sup>0</sup>, Ni<sup>2+</sup>, shake-up peaks in the Ni 2*p*<sub>3/2</sub> region<sup>9,10,35</sup>. Following sequential treatments with H<sub>2</sub> and 25 vol% CO<sub>2</sub>/H<sub>2</sub>, Ni species transitioned from NiO (Ni<sup>2+</sup>) to Ni<sub>3</sub>In (Ni<sup>0</sup>) and further to the Ni<sub>3</sub>InC<sub>0.5</sub> phase (Ni<sup>0</sup>). These transformations were also observed by the C 1*s* spectra, where the appearance of a Ni-C peak at 283.2 eV followed the vanishing of the C-O peak at 286.0 eV, the decline and later intensification of the C=O peak at 289.0 eV corresponding to the surface carbonate groups<sup>28,36,37</sup>. In the In 3*d* spectra, peaks with BE of 444.5 eV and 452.1 eV correspond to the oxidative state (In<sup>3+</sup>) of In 3*d*<sub>5/2</sub> and 3*d*<sub>3/2</sub>, respectively, while peaks for In<sup>0</sup> species are located at 443.3 and 450.9 eV<sup>28,38</sup>. The presence of In<sup>3+</sup> peaks in the reduced sample may stem from small amounts of unreduced In<sub>2</sub>O<sub>3</sub> strongly interacting with the support at a low reduction temperature of 400 °C, or from intercalated In<sub>2</sub>O<sub>3</sub> species located between the NiIn IMC and the ZrO<sub>2</sub> support<sup>39,40</sup>. More importantly, the increased peak area for In<sup>3+</sup> after carburization, along with a rise in the O 1*s* peak area at 531.2 eV, indicates In oxidation and a concentration increase in oxygen vacancy<sup>9,38</sup>, suggesting the formation of a sub-stoichiometric, defective In<sub>2</sub>O<sub>3-x</sub> overlayer containing abundant oxygen vacancies. The same variation trend in the proportion of surface In<sup>3+</sup> species was also observed from the unsupported NiO/In<sub>2</sub>O<sub>3</sub> (NiInO), NiInZrO, and NiInCZr samples after exposure to CO<sub>2</sub>/H<sub>2</sub> (1:3) atmosphere, following sequential H<sub>2</sub> and CO/H<sub>2</sub> (1:2) treatments during in-situ XPS experiments (Fig. 2f and Supplementary 15).

Moreover, the content of In<sub>2</sub>O<sub>3</sub> species was found to be tunable by adjusting the CO<sub>2</sub> concentration within the CO/CO<sub>2</sub>/H<sub>2</sub> feed gas during the synthesis of NiInCZr catalysts. As revealed by the quasi-in-situ XPS In 3*d* spectra, the proportion of surface In<sup>3+</sup> species increased with rising CO<sub>2</sub> concentration, with the NiInCZr sample synthesized under CO<sub>2</sub>/H<sub>2</sub> (1:2) exhibiting the highest amount (Fig. 2g and Supplementary 16). These findings were further supported by H<sub>2</sub>-TPR coupled with MS analysis, wherein the NiInCZr-CO<sub>2</sub>/H<sub>2</sub> sample showed the most prominent H<sub>2</sub>O signal peak at ~500 °C, corresponding to the reduction of surface In<sub>2</sub>O<sub>3</sub> species (Fig. 2h and Supplementary 17). Collectively, these results strongly suggest that CO<sub>2</sub> might act as the driving force for selective surface oxidation of Ni<sub>3</sub>InC<sub>0.5</sub>, leading to the formation of In<sub>2</sub>O<sub>3-x</sub> overlayers.

### CO<sub>2</sub>-induced in exsolution and inverse In<sub>2</sub>O<sub>3-x</sub>/Ni interfaces

Given the critical role of CO<sub>2</sub> in selective surface oxidation, two oxidation experiments were conducted on NiInZr and NiInCZr catalysts, each exposed to one of the oxidative components involved in the RWGS reaction, CO<sub>2</sub> and H<sub>2</sub>O, respectively, without H<sub>2</sub> co-feeding.

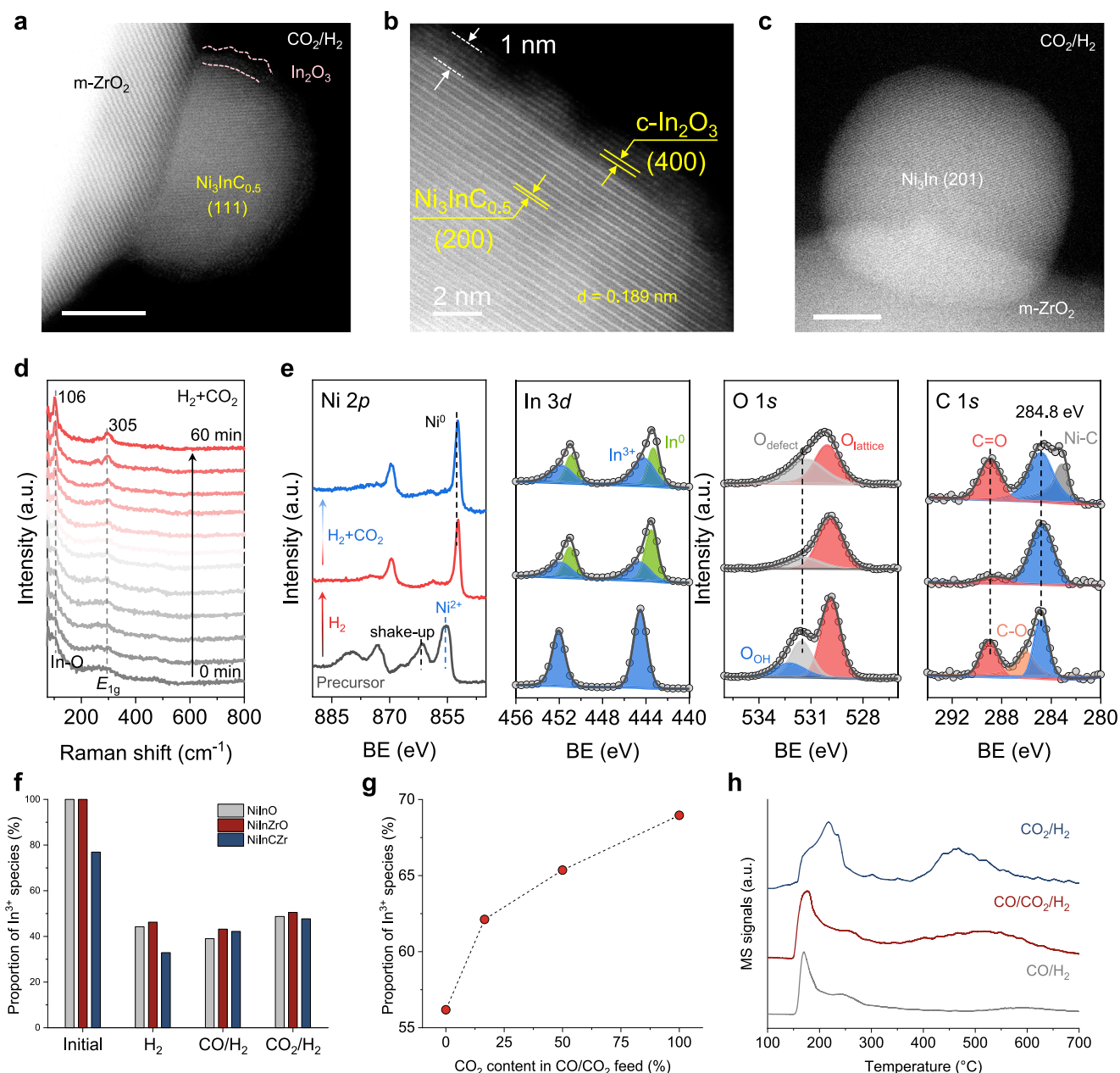


**Fig. 2 | In-situ characterizations on the formation of In<sub>2</sub>O<sub>3-x</sub> overlayers. a** Quasi-in-situ AC-HAADF-STEM image of the NiInCZr catalyst transferred using glove boxes and Mel-Build Double tilt Atmos Defend holder. **b** Enlarged AC-HAADF-STEM image of the fresh NiInCZr catalyst. **c** In-situ AC-HAADF-STEM image of a supported Ni<sub>3</sub>In NP after one and a half hours of reaction. **d** In-situ Raman spectra of the unsupported Ni<sub>3</sub>InC<sub>0.5</sub> sample under 25 vol% CO<sub>2</sub>/H<sub>2</sub> atmosphere, 400 °C, 1 bar. **e** In-situ Ni 3d, In 3d, O 1s, and C 1s XPS spectra of the NiInZrO precursor treated by

H<sub>2</sub> then 25 vol% CO<sub>2</sub>/H<sub>2</sub> at 400 °C, 1 bar. BE: binding energy. **f, g** Proportion of surface In<sup>3+</sup> species calculated from XPS In 3d spectra: NiInO, NiInZrO, and NiInCZr sample subjected to a sequential in-situ XPS experiment (**f**) and NiInCZr catalysts synthesized under different CO/CO<sub>2</sub>/H<sub>2</sub> atmosphere (**g**). **h** H<sub>2</sub>O signals from H<sub>2</sub>-TPR coupled with MS corresponding to NiInCZr catalysts synthesized under the same conditions. CO/CO<sub>2</sub>/H<sub>2</sub> gas used: CO/H<sub>2</sub> (1:2), CO/CO<sub>2</sub>/H<sub>2</sub> (3:3:14), and CO<sub>2</sub>/H<sub>2</sub> (1:3).

Upon CO<sub>2</sub> oxidation, the NiInZr catalyst developed a significant amount of crystalline c-In<sub>2</sub>O<sub>3</sub> species assembled on the surface of the NiIn IMC NPs, with no detectable NiO phase (Supplementary Figs. 18a and 19a, b). As expected, Ni 2p spectra showed no significant changes, whereas metallic In was fully oxidized to In<sup>3+</sup> (Supplementary Fig. 19c). In contrast, the NiInCZr catalyst exhibited greater structural stability under identical conditions. However, XPS still detected a moderate increase in surface In<sup>3+</sup> content. To sum up, CO<sub>2</sub> can preferentially oxidize In when In alloys with Ni to form Ni<sub>3</sub>In and Ni<sub>3</sub>InC<sub>0.5</sub>, consistent with thermodynamic analysis of CO<sub>2</sub> oxidation for Ni and In (Supplementary Fig. 18b).

On the contrary, H<sub>2</sub>O exhibits a stronger oxidation ability, simultaneously oxidizing both surface Ni and Integrating these findings with the Ni-In binary phase diagram<sup>41</sup>, we propose that In atoms exsolve from the surface of NiIn species (IMC and carbide), leaving behind a Ni-rich layer between the NiIn core and the In<sub>2</sub>O<sub>3-x</sub> shell, thereby forming an inverse In<sub>2</sub>O<sub>3-x</sub>/Ni interface. In the NiIn IMC and carbide catalysts (Supplementary Fig. 20).

To further validate the formation of the inverse In<sub>2</sub>O<sub>3</sub>/Ni structure, quasi-in-situ and in-situ X-ray absorption spectroscopy (XAS) were performed on the NiIn-based catalysts. As shown in Fig. 3a, b and Supplementary Table 5, X-ray absorption near edge structure (XANES),

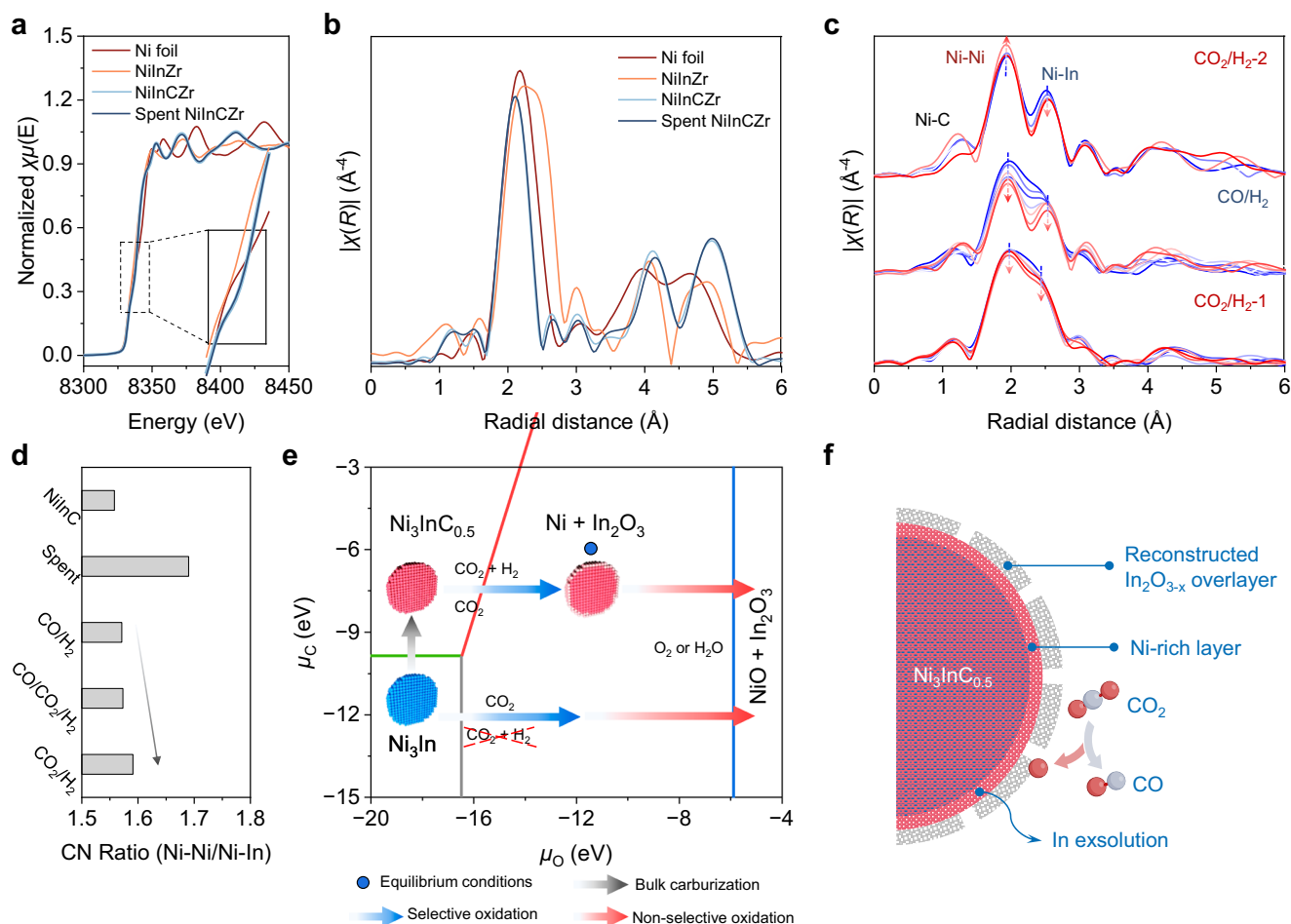


**Fig. 3 | Inverse  $\text{In}_2\text{O}_{3-x}/\text{Ni}$  interfaces from  $\text{CO}_2$ -induced selective surface oxidation.** **a, b** Investigation of the coordination of NiInCZr and referenced samples: Ni  $K$ -edge XANES (**a**) and EXAFS spectra (**b**). All samples were transferred through a glove box and sealed with tape before test. **c** In-situ Fourier transformed  $k^2$ -weighted Ni-EXAFS spectra of the NiInZrO precursor with atmosphere changing from  $\text{CO}_2/\text{H}_2$  to  $\text{CO}/\text{H}_2$  to  $\text{CO}_2/\text{H}_2$ . Conditions:  $400^\circ\text{C}$ , 1 bar. **d** CN ratio of Ni-Ni path

to Ni-In path over different  $\text{Ni}_3\text{InC}_{0.5}$ -based catalyst. NiInC: unsupported  $\text{Ni}_3\text{InC}_{0.5}$ ; Spent: spent NiInCZr;  $\text{CO}/\text{H}_2$ ,  $\text{CO}/\text{CO}_2/\text{H}_2$ ,  $\text{CO}_2/\text{H}_2$  represent the NiInCZr sample synthesized using corresponding gas. **e** Computed phase diagram of  $\text{Ni}_3\text{In}$ ,  $\text{Ni}_3\text{InC}_{0.5}$ ,  $\text{Ni} + \text{In}_2\text{O}_3$ , and  $\text{NiO} + \text{In}_2\text{O}_3$  with each solid line indicating phase equilibrium between two species. **f** Schematic illustration of the inverse  $\text{In}_2\text{O}_{3-x}/\text{Ni}$  interface structure.

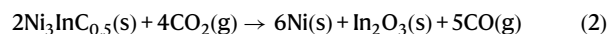
R-space extended X-ray absorption fine structure (EXAFS) spectra, and corresponding first-shell coordination fitting reveal that Ni in all NiIn carbide samples remains in a metallic state, coordinated by Ni-C, Ni-Ni, and Ni-In paths. Compared with Ni foil, the positive shift in absorption edge and the enhanced white line intensity indicate an electron-deficient character of Ni atoms in both fresh and spent NiInCZr samples<sup>42,43</sup>, consistent with XPS analysis (Supplementary Fig. 11).

In-situ XAS measurements under sequential gas treatment ( $\text{H}_2$ ,  $\text{CO}_2/\text{H}_2$ ,  $\text{CO}/\text{H}_2$ , and again  $\text{CO}_2/\text{H}_2$ ) provided direct insight into In exsolution and Ni-rich layer formation (Fig. 3c and Supplementary Fig. 21). After carburization in  $\text{CO}_2/\text{H}_2$  and  $\text{CO}/\text{H}_2$ , subsequent  $\text{CO}_2/\text{H}_2$  treatment induced surface oxidation. The observed peak sharpening during these processes indicates enhanced short-range order of the NiInC carbide compared to the NiIn alloy, reflecting higher crystallinity. Moreover, the increasing intensity of the Ni-Ni path, accompanied by a decreasing Ni-In path, supports the formation of an  $\text{In}_2\text{O}_3$  overlayer via In atoms exsolution from the  $\text{Ni}_3\text{InC}_{0.5}$  surface, leaving a Ni-rich layer underneath and yielding an inverse  $\text{In}_2\text{O}_{3-x}/\text{Ni}$  interface.

Further evidence was provided by EXAFS spectra and coordination number (CN) fitting of NiInCZr catalysts synthesized under various  $\text{CO}/\text{CO}_2/\text{H}_2$  atmospheres (Supplementary Figs. 22, 23 and Table 5). Compared to the benchmark unsupported NiInC sample, catalysts prepared with higher  $\text{CO}_2$  content exhibited a higher CN ratio ( $R_{\text{CN}}$ ) of Ni-Ni path to Ni-In path (Fig. 3d). This trend indicates an increase in

both the Ni-rich layer and  $\text{In}_2\text{O}_3$  overlayer content, reaffirming that  $\text{CO}_2$  promotes selective surface oxidation and facilitates inverse  $\text{In}_2\text{O}_3/\text{Ni}$  interface formation.

Phase diagram of the NiIn-based system, calculated as a function of chemical potentials of carbon ( $\mu_{\text{C}}$ ) and oxygen ( $\mu_{\text{O}}$ ), provide additional theoretical support for the formation of this inverse structure (Fig. 3e). Under the  $\text{CO}_2/\text{CO}/\text{H}_2$  atmosphere, bulk carburization is thermodynamically favored over surface oxidation on  $\text{Ni}_3\text{In}$ , as the reducing power of  $\text{H}_2$  outweighs the oxidizing effect of  $\text{CO}_2$ . According to Eq. (2),  $\text{CO}_2$  selectively oxidizes the surface of the  $\text{Ni}_3\text{InC}_{0.5}$  phase upon its formation. Ultimately, under the equilibrium conditions, the phase settles in the Ni and  $\text{In}_2\text{O}_3$  domain on the phase diagram, consistent with the inverse  $\text{In}_2\text{O}_{3-x}/\text{Ni}$  interface structure



Taken together, the  $\text{CO}_2$  oxidation behaviors of NiInZr and NiInCZr elucidate the mechanism of selective oxidation on the  $\text{Ni}_3\text{InC}_{0.5}$  surface: during the RWGS reaction,  $\text{CO}_2$  initiates the reverse Boudouard reaction (Eq. (2)), releasing oxygen atoms to the surface and promoting selective oxidation of In. With continued In exsolution, the remaining Ni atoms form a Ni-rich layer between the  $\text{Ni}_3\text{InC}_{0.5}$  core and the  $\text{In}_2\text{O}_{3-x}$  overlayer, thus creating an inverse  $\text{In}_2\text{O}_{3-x}/\text{Ni}$  interface (Fig. 3f).

**Catalytic performance and structure-activity relationship**

To assess the roles of  $\text{In}_2\text{O}_{3-x}$  overlayers and inverse  $\text{In}_2\text{O}_{3-x}/\text{Ni}$  interfaces on  $\text{CO}_2$  hydrogenation to methanol, supported  $\text{Ni}_3\text{InC}_{0.5}$  and the other referenced catalysts were evaluated under reaction conditions of 4 MPa,  $\text{H}_2/\text{CO}_2/\text{N}_2 = 72:24:4$ , and a weight hourly space velocity (WHSV) of  $12,000 \text{ mL g}_{\text{cat}}^{-1} \text{ h}^{-1}$ , unless otherwise specified.

The  $\text{NiInCZr}$  catalyst exhibited good activity for  $\text{CO}_2$  hydrogenation to methanol, surpassing the selectivity limitations of traditional Ni-based catalysts that favor  $\text{CH}_4$ <sup>44,45</sup> and  $\text{CO}$ <sup>2,46</sup> production (Fig. 4a, b and Supplementary Figs. 24–26). Specifically,  $\text{NiInCZr}$  reached a  $\text{CO}_2$  conversion ( $X_{\text{CO}_2}$ ) of ca. 9% at 300 °C, while its methanol selectivity ( $S_{\text{MeOH}}$ ) showed an inverse trend as the temperature increased. Both

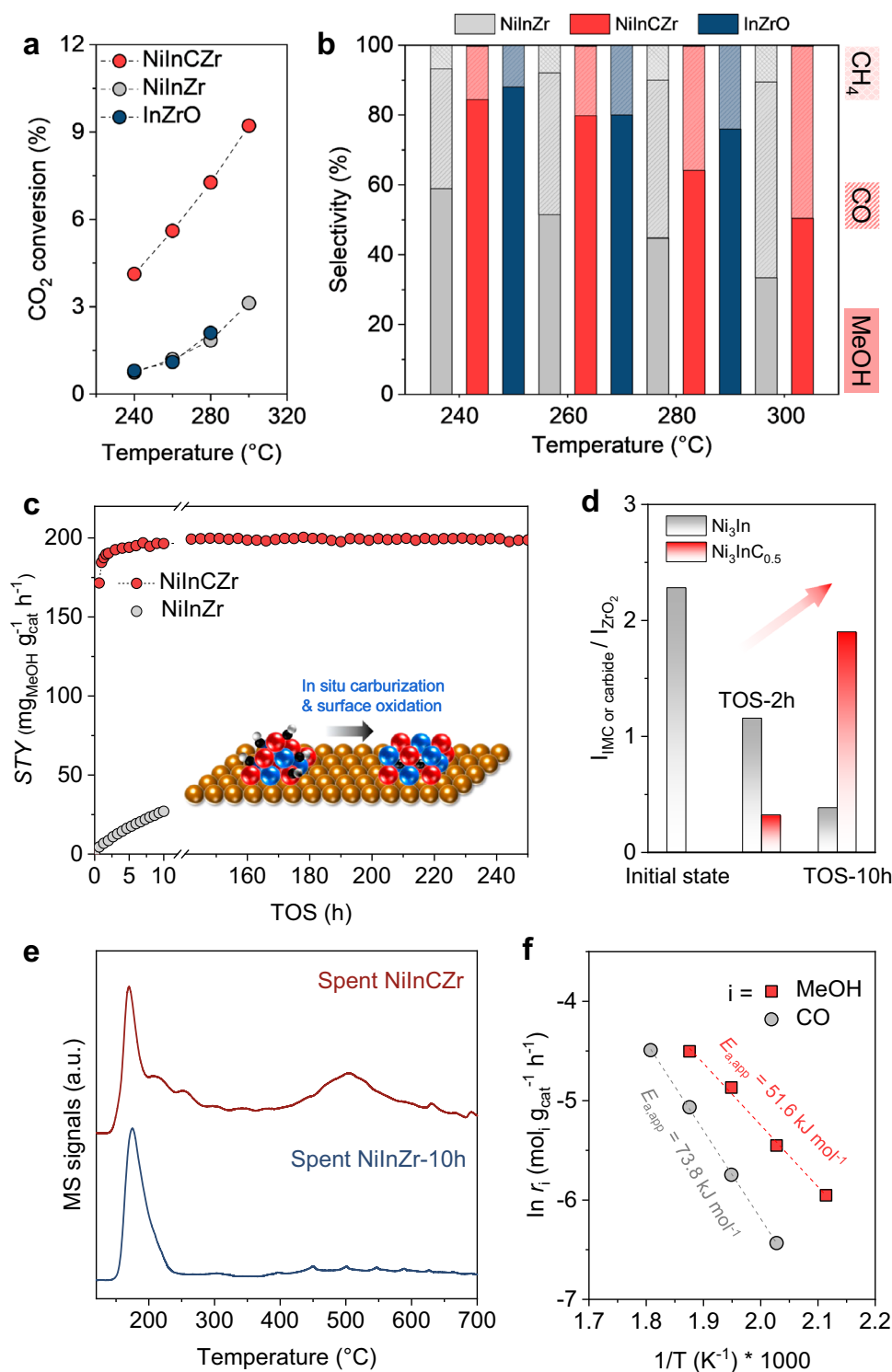


**Fig. 4 | Catalytic performance of  $\text{CO}_2$  hydrogenation over the supported  $\text{Ni}_3\text{InC}_{0.5}$  catalyst.** **a–c** Catalytic performance:  $\text{CO}_2$  conversion (**a**), selectivity (**b**), stability at 280 °C (**c**). Insets in (**c**) is the illustration of in-situ carburization and surface oxidation over the  $\text{Ni}_3\text{In}$  IMC phase during the reaction. **d** Relative content of two active phases in the  $\text{NiInZr}$  catalyst at different TOS determined by XRD

analysis. The (201) of  $\text{Ni}_3\text{In}$  and (111) of  $\text{Ni}_3\text{InC}_{0.5}$  chosen as the representative planes were normalized by (111) of  $m\text{-ZrO}_2$ . TOS: time-on-stream. **e**  $\text{H}_2\text{O}$  signals from  $\text{H}_2$ -TPR coupled with MS corresponding to spent  $\text{NiInCZr}$  and  $\text{NiInZr-10h}$  samples. **f** Arrhenius plots of the  $\text{Ni}_3\text{InC}_{0.5}$  catalyst.  $\text{InZrO}$ :  $\text{ZrO}_2$  supported  $\text{In}_2\text{O}_3$  catalyst. Standard evaluation conditions: 4 MPa,  $\text{CO}_2/\text{H}_2 = 1:3$ , WHSV of  $12,000 \text{ mL g}_{\text{cat}}^{-1} \text{ h}^{-1}$ .

parameters were consistently higher across all temperatures than those of NiInZr. Consequently, the methanol space-time yield ( $STY_{MeOH}$ ) exhibited a volcano-shaped profile, peaking at  $193.6 \text{ mg g}_{\text{cat}}^{-1} \text{ h}^{-1}$  at  $280^\circ\text{C}$  with 7% of  $X_{\text{CO}_2}$  and 70% of  $S_{\text{MeOH}}$ . Even in the absence of support effects, unsupported NiInC maintained methanol selectivity above 80% (Supplementary Fig. 27).

During the long-term stability test, the NiInCZr catalyst exhibited a rapid increase in performance initially and remained stable within 250 h in terms of  $X_{\text{CO}_2}$ ,  $S_{\text{MeOH}}$ , and  $STY_{\text{MeOH}}$ , surpassing most of the  $\text{In}_2\text{O}_3$ -based catalysts, as well as the commercial Cu-based catalyst for  $\text{CO}_2$ -to-methanol (Fig. 4c, Supplementary Fig. 28 and Table 6)<sup>16,47,48</sup>. As anticipated, the spent NiInCZr catalyst maintained a stable bulk crystal structure, with no observable new peaks emerging or peak shifting in the XRD pattern (Supplementary Fig. 29). Besides, the AC-HAADF-STEM image displayed the well-preserved  $\text{In}_2\text{O}_{3-x}$  overlayer structure after the long-term reaction (Supplementary Fig. 30). From XPS spectra, Ni remained in the metallic state, while the content of oxidative In increased slightly (Supplementary Fig. 31). These results demonstrate the high stability of the inverse  $\text{In}_2\text{O}_{3-x}/\text{Ni}$  structures on the  $\text{Ni}_3\text{InC}_{0.5}$  phase, addressing the inherent shortcomings of the metal-promoted  $\text{In}_2\text{O}_3$  catalysts<sup>20,21,47,48</sup>.

As for the NiInZr catalyst, its  $STY_{\text{MeOH}}$ , as well as  $X_{\text{CO}_2}$  and  $S_{\text{MeOH}}$ , started with ultra-low values and continued to increase within 10 h on stream, hinting at its persistent structural evolution to form active species (Fig. 4c and Supplementary Fig. 28). According to its XRD patterns at a different time on stream (TOS), a phase transformation from  $\text{Ni}_3\text{In}$  to  $\text{Ni}_3\text{InC}_{0.5}$  was found over time (Fig. 4d and Supplementary Fig. 32), which was also observed with the unsupported  $\text{Ni}_3\text{In}$  catalyst during the long-term stability test (Supplementary Fig. 33). Furthermore, the HRTEM image of the NiInZr TOS-2h sample exhibited a half-transformed state of a supported  $\text{Ni}_3\text{In}$  NP after 2 h of the reaction (Supplementary Fig. 32b), characterized by a distinct grain boundary between the  $\text{Ni}_3\text{In}$  (102) and  $\text{Ni}_3\text{InC}_{0.5}$  (200) planes. Analysis of the  $\text{H}_2$ -TPR coupled with MS reveals that the NiInZr-10 h sample exhibits only a minor  $\text{H}_2\text{O}$  signal peak at  $-500^\circ\text{C}$ , corresponding to the reduction of  $\text{In}_2\text{O}_3$  species (Fig. 4e). This low signal intensity, indicative of limited  $\text{In}_2\text{O}_3$  content and IMC-like surface, correlates with the incomplete carburization and further highlights the critical roles of  $\text{In}_2\text{O}_{3-x}$  overlayers and inverse  $\text{In}_2\text{O}_{3-x}/\text{Ni}$  interfaces in  $\text{CO}_2$  hydrogenation to methanol, as well as the sequence order of the bulk carburization and surface oxidation. The catalytic performance at the beginning two hours of catalyst evaluation tests over the NiInCZr catalysts synthesized under various  $\text{CO}/\text{CO}_2/\text{H}_2$ -containing atmospheres again approve this conclusion (Supplementary Fig. 34).

Kinetic studies give a deeper understanding of the structure-activity relationship. External diffusion effect was eliminated by varying the WHSV applied (Supplementary Fig. 35). The extracted apparent activation energy ( $E_{a,\text{app}}$ ) values show that NiInCZr has the lowest  $E_{a,\text{app}}$  for methanol formation ( $51.6 \text{ kJ mol}^{-1}$ ) and the highest for CO ( $73.8 \text{ kJ mol}^{-1}$ ), correlating with the highest  $S_{\text{MeOH}}$  and lowest  $S_{\text{CO}}$  (Fig. 4f and Supplementary Fig. 36). Reaction orders ( $n_i$ ) with respect to  $\text{CO}_2$  and  $\text{H}_2$ , which reflects surface reactant coverage<sup>22,49</sup>, indicate that NiInCZr has a superior  $\text{CO}_2$  adsorption/activation ability ( $n_{\text{CO}_2} = 0.14$ ), despite its comparatively low H coverage ( $n_{\text{H}_2} = 1.39$ ) (Supplementary Fig. 37). Besides, the  $\text{H}_2$  reaction order for NiInCZr showed an unusual trend: the methanol formation rate ( $r_{\text{MeOH}}$ ) increased as the  $\text{H}_2/\text{CO}_2$  ratio ( $R_{\text{H}_2/\text{CO}_2}$ ) raised from 3 to 3.5, displaying a positive  $n_{\text{H}_2}$ . However, beyond an  $R_{\text{H}_2/\text{CO}_2}$  of 3.5, further increases in  $\text{H}_2$  partial pressure led to a sharp decline in  $r_{\text{MeOH}}$ , resulting in a negative  $n_{\text{H}_2}$ , contrary to conventional  $\text{CO}_2$  hydrogenation behavior<sup>22,49,50</sup>. Considering the surface structure of the  $\text{Ni}_3\text{InC}_{0.5}$  NPs, we surmise that the abnormal upheaval in  $\text{H}_2$  reaction order should be attributed to the degradation of  $\text{In}_2\text{O}_{3-x}$  overlayers under elevated  $\text{H}_2$  partial pressures<sup>47</sup>.

Similar conclusions could be drawn from the temperature-programmed desorption (TPD) tests (Supplementary Figs. 38 and 39).

From  $\text{CO}_2$ -TPD profiles, NiInCZr displayed more medium and strong basic sites for  $\text{CO}_2$  adsorption than NiInZr and the m-ZrO<sub>2</sub> support<sup>51</sup>. Due to the presence of  $\text{In}_2\text{O}_{3-x}$  overlayer, it can provide extra active sites for  $\text{CO}_2$  activation on  $\text{Ni}_3\text{InC}_{0.5}$  NPs<sup>22,38,47</sup>, accounting for the enhanced  $X_{\text{CO}_2}$  over the NiInCZr catalyst. Therefore, even without support,  $\text{Ni}_3\text{InC}_{0.5}$  remains more effective for  $\text{CO}_2$  hydrogenation to methanol than the NiInZr catalyst (Supplementary Fig. 27). On the other hand,  $\text{H}_2$ -TPD analysis indicates poorer  $\text{H}_2$  activation over  $\text{Ni}_3\text{InC}_{0.5}$  than  $\text{Ni}_3\text{In}$  IMC. Both  $\text{CO}_2$  and  $\text{H}_2$ -TPD results are consistent with the low  $\text{H}_2$  and high  $\text{CO}_2$  coverage inferred from the kinetic studies, owing to the presence of the defective  $\text{In}_2\text{O}_{3-x}$  overlayers.

To further enhance the catalytic performance of  $\text{Ni}_3\text{InC}_{0.5}$ -based catalysts for  $\text{CO}_2$  to methanol, we optimized the oxide support and identified  $\text{Al}_2\text{O}_3$  as the most effective option (Supplementary Fig. 40 and Table 7). Given that layered double hydroxides (LDHs) are excellent precursors for achieving high dispersion of active species on  $\text{Al}_2\text{O}_3$  support<sup>52,53</sup>, we subsequently developed an LDH-derived  $\text{Al}_2\text{O}_3$ -supported NiIn carbide catalyst (LDH-NiInCAI). This catalyst achieved an  $X_{\text{CO}_2}$  of 19% and  $S_{\text{MeOH}}$  of 65%, with a  $STY_{\text{MeOH}}$  of  $508.4 \text{ mg g}_{\text{cat}}^{-1} \text{ h}^{-1}$  at  $260^\circ\text{C}$ , 5 MPa, and  $12,000 \text{ mL g}_{\text{cat}}^{-1} \text{ h}^{-1}$ , surpassing the commercial CZA catalysts and ranking among the state-of-the-art catalysts reported, including noble metal-based catalysts, showing great promising for industrial application (Supplementary Fig. 41 and Table 8).

## Reaction mechanisms and active sites

Fundamental knowledge of the underlying reaction mechanisms and active sites of the  $\text{Ni}_3\text{InC}_{0.5}$  phase was investigated by in-situ transient Fourier transform infrared spectroscopy (FTIR) performed at  $280^\circ\text{C}$ , 2 MPa, for the NiInCZr catalyst. Detailed vibration band assignments for surface species are listed in Supplementary Table 9.

During  $\text{CO}_2$  adsorption, monodentate carbonate ( $\text{m-CO}_3^*$ ,  $1398$  and  $1495 \text{ cm}^{-1}$ )<sup>54–56</sup> dominated at 0.1 MPa, with some ionic bicarbonate species ( $\text{i-HCO}_3^*$ , at  $1420 \text{ cm}^{-1}$ )<sup>57</sup> forming as well (Fig. 5a). Since  $\text{ZrO}_2$  and  $\text{In}_2\text{O}_3$  species are the only two candidates for  $\text{CO}_2$  adsorption on NiInCZr catalyst, the distinct  $\text{CO}_2$  adsorption profile of m-ZrO<sub>2</sub> (b- $\text{CO}_3^*$ ) demonstrate that the  $\text{In}_2\text{O}_{3-x}$  overlayer serves as the primary sites for  $\text{CO}_2$  activation (Supplementary Fig. 42). This conclusion is consistent with both the kinetic and chemisorption results. At 2 MPa, m- $\text{CO}_3^*$  intensified, and small amounts of formate species ( $\text{HCOO}^*$ , ca.  $1585 \text{ cm}^{-1}$ ) formed via hydrogenation of carbonate by surface hydrides (Ni-H or In-H). The observed bands at  $2150$ – $1850 \text{ cm}^{-1}$  and  $1100$ – $1000 \text{ cm}^{-1}$ , e.g., the signals at  $2077$ ,  $2055$ ,  $1080$ , and  $1050 \text{ cm}^{-1}$ , are assigned to gas-phase  $\text{CO}_2$ , rather than adsorbed  $\text{CO}^*$  species from  $\text{CO}_2$  dissociation<sup>58,59</sup>.

Upon switching to  $\text{H}_2$ , m- $\text{CO}_3^*$  bands gradually faded, accompanied by the emergence of bidentate formate (bi- $\text{HCOO}^*$ , located between  $1600$ – $1300 \text{ cm}^{-1}$ ), linearly bonded carbonyl ( $\text{CO}^*$  on exposed Ni sites, at  $2022 \text{ cm}^{-1}$ )<sup>60</sup>, and methoxy ( $\text{H}_3\text{CO}^*$ , at  $1146$  and  $1075 \text{ cm}^{-1}$ ) species, along with a decline in the gaseous  $\text{CO}_2$  signals. Similar to the behavior of the  $\text{ZnZrO}_x$  catalyst<sup>57</sup>, NiInCZr exhibited bi- $\text{HCOO}^*$  adsorbed on adjacent In and Ni sites at the inverse  $\text{In}_2\text{O}_{3-x}/\text{Ni}$  interfaces (bi- $\text{HCOO-In-Ni}$ , at  $1595$ ,  $1347$ , and  $1318 \text{ cm}^{-1}$ ), while bands at  $1578$ ,  $1382$ , and  $1371 \text{ cm}^{-1}$  correspond to bi- $\text{HCOO}^*$  adsorbed on neighboring In sites on the  $\text{In}_2\text{O}_{3-x}$  overlayers (bi- $\text{HCOO-In-In}$ )<sup>55,56,61–64</sup>. Identical in-situ FTIR spectra of the unsupported NiInC catalyst further support the presence of these two active site configurations (Supplementary Fig. 43).

To assess their relevance to methanol synthesis, formate species consumption was tracked under  $\text{H}_2$  flow after saturating the NiInCZr catalyst surface with intermediates in the 25 vol%  $\text{CO}_2/\text{H}_2$  atmosphere. During  $\text{CO}_2$  hydrogenation, the consumption of m- $\text{CO}_3^*$  and formation of bi- $\text{HCOO}^*$ ,  $\text{H}_3\text{CO}^*$ , and  $\text{CO}^*$  were observed until the system reached a steady state (Supplementary Fig. 44a, b). When the mixed gas (25 vol%  $\text{CO}_2/\text{H}_2$ ) was replaced with  $\text{H}_2$ , formate species, and gaseous  $\text{CO}_2$  declined, while  $\text{CO}^*$  remained stable, indicating that methanol

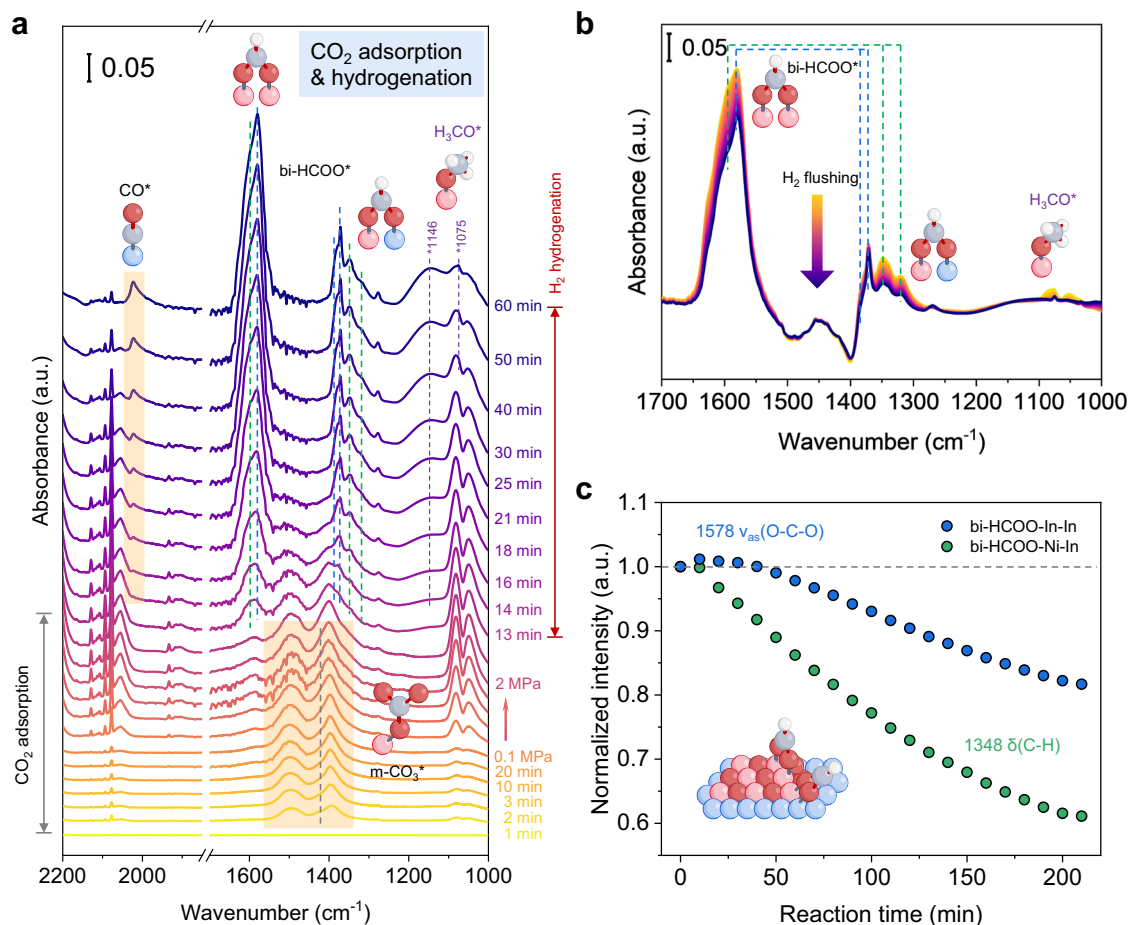


**Fig. 5 | Identifying active sites and reaction mechanisms of  $\text{Ni}_3\text{InC}_{0.5}$  carbide catalyst.** **a, b** High-pressure in-situ FTIR spectra:  $\text{CO}_2$  adsorption and subsequent  $\text{H}_2$  hydrogenation (**a**),  $\text{H}_2$  flushing post- $\text{CO}_2$  hydrogenation (**b**). **c** Corresponding normalized IR intensities of various species versus reaction time during the  $\text{H}_2$  flushing

process. Reaction conditions: 2 MPa, 280 °C, 30 mL  $\text{min}^{-1}$  of reactant gas ( $\text{H}_2:\text{CO}_2 = 3:1$ ). Intensity normalization was calculated based on the highest intensity value of the specific species. Assignments of ball models: blue (Ni), pink (In), gray (C), red (O), and white (H).

synthesis follows the formate pathway (Supplementary Fig. 44c and Fig. 5b). Notably, the consumption rates of the two formate species differ significantly. According to normalized intensity over time, bi-HCOO-In-In at 1578  $\text{cm}^{-1}$  peaked and then declined, while bi-HCOO-Ni-In at 1348  $\text{cm}^{-1}$  continued to decrease throughout the process (Fig. 5c). This result shows that the hydrogenation rate of bi-HCOO\* at the Ni-In sites is much faster than at In-In sites. The asymmetric Ni-In sites at the inverse  $\text{In}_2\text{O}_{3-x}/\text{Ni}$  interfaces are more active for methanol formation in the NiInCZr catalyst. A similar trend could also be observed from the in-situ FTIR spectra at different reaction temperatures, where elevated temperatures led to a visibly faster decrease in bi-HCOO-Ni-In intensity than that of the bi-HCOO-In-In (Supplementary Fig. 45).

In conclusion, two types of active sites contribute to the high methanol selectivity of the NiInCZr catalyst: (1) the  $\text{In}_2\text{O}_{3-x}$  overlayers, which facilitate  $\text{CO}_2$  activation and perform the hydrogenation resembling conventional  $\text{In}_2\text{O}_3$ -based catalysts; and (2) the inverse  $\text{In}_2\text{O}_{3-x}/\text{Ni}$  interfaces, where Ni promotes the hydrogenation of formate species in cooperation with adjacent In (asymmetric Ni-In site).

### Theoretical descriptions of reaction mechanisms

To deepen the understanding of the structure-dependent activity of the  $\text{Ni}_3\text{InC}_{0.5}$  phase for  $\text{CO}_2$  hydrogenation to methanol, density functional theory (DFT) calculations were conducted. Surface models of  $\text{Ni}_3\text{In}$  (111),  $\text{Ni}_3\text{InC}_{0.5}$  (111), cubic  $\text{In}_2\text{O}_3$  with an exposed (100) plane, and  $\text{In}_2\text{O}_3$  clusters on Ni (111) ( $\text{In}_2\text{O}_3/\text{Ni}$ ) were constructed to simulate the  $\text{Ni}_3\text{In}$  IMC,  $\text{Ni}_3\text{InC}_{0.5}$ , and the two active sites of the selectively

oxidized  $\text{Ni}_3\text{InC}_{0.5}$  phase: In-In sites on  $\text{In}_2\text{O}_{3-x}$  overlayers and asymmetric Ni-In sites at the inverse  $\text{In}_2\text{O}_{3-x}/\text{Ni}$  interfaces, respectively (Supplementary Fig. 46).

For  $\text{CO}_2$  activation, the adsorption mechanism varied among the models. On the  $\text{In}_2\text{O}_3$  and  $\text{In}_2\text{O}_3/\text{Ni}$  models,  $\text{CO}_2$  adsorbs via its C atom binding to the lattice oxygen on the  $\text{In}_2\text{O}_3$  surface, while one of its O atoms interacts with the In atom ( $m-\text{CO}_3^*$  configuration, Supplementary Fig. 47). In contrast, physical adsorption occurred on the  $\text{Ni}_3\text{In}$  and  $\text{Ni}_3\text{InC}_{0.5}$  models. The calculated adsorption energies were higher on  $\text{In}_2\text{O}_3$ -related structures, particularly  $c\text{-In}_2\text{O}_3$  ( $-0.90$  eV), align with  $\text{CO}_2$ -TPD and kinetics studies, validating the enhanced  $\text{CO}_2$  activation ability of the selectively oxidized  $\text{Ni}_3\text{InC}_{0.5}$  phase. Both  $\text{In}_2\text{O}_{3-x}$  overlayers and inverse  $\text{In}_2\text{O}_{3-x}/\text{Ni}$  interfaces contribute key active sites for  $\text{CO}_2$  activation.

For  $\text{H}_2$  activation, heterolytic dissociation occurred on the  $\text{In}_2\text{O}_3$  model with an activation energy ( $E_a$ ) of 0.39 eV, forming hydroxyl (O-H) and hydridic H (In-H) species (Supplementary Fig. 48)<sup>17</sup>. In contrast, homolytic  $\text{H}_2$  dissociation on the Ni (111) surface was nearly barrierless ( $E_a = 0.01$  eV)<sup>65</sup>. These results suggest that the exposed Ni sites at the inverse  $\text{In}_2\text{O}_{3-x}/\text{Ni}$  interfaces, in addition to the conventional active sites on  $\text{In}_2\text{O}_{3-x}$  overlayers, offer a stronger  $\text{H}_2$  activation capability.

The formate mechanism for methanol synthesis was further analyzed to compare the activities of In-In and Ni-In sites (Fig. 6 and Supplementary Table 10–12). The initial step involves the hydrogenation of  $m-\text{CO}_3^*$  to bi-HCOO\*. On the oxide overlayer, proton-like H from  $\text{In}_2\text{O}_3$  drives this hydrogenation with an  $E_a$  of 1.50 eV, while at the

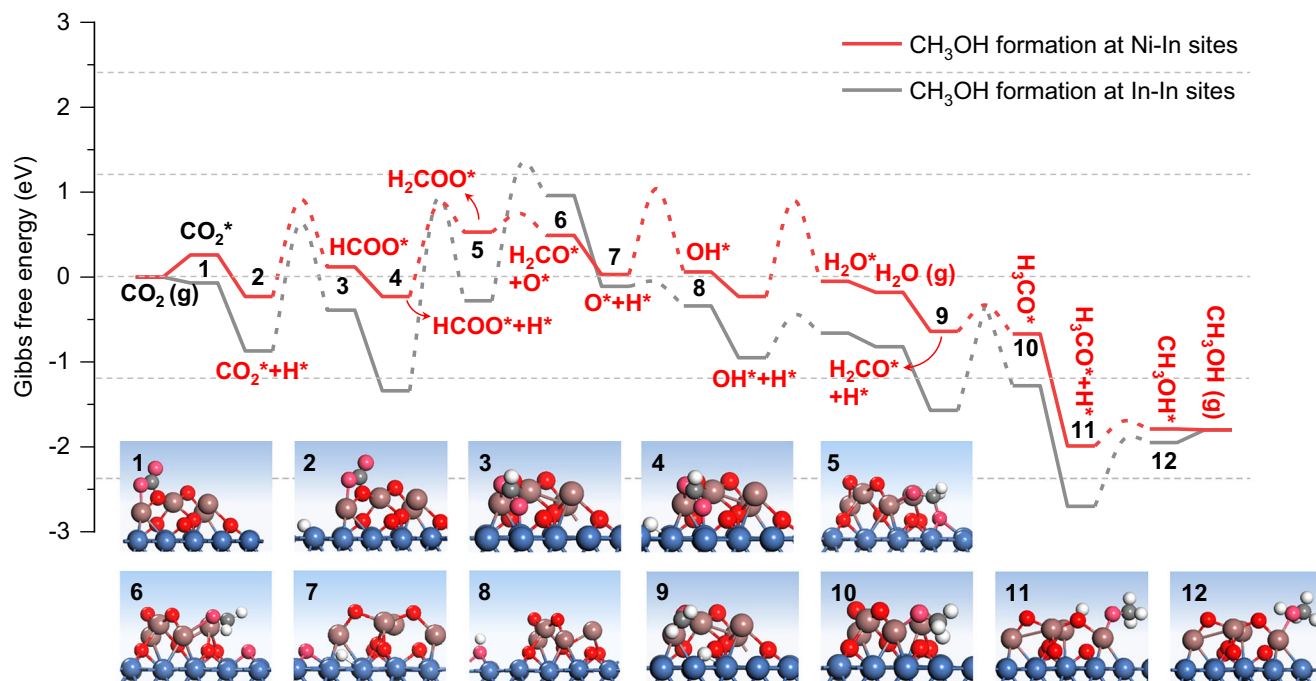


**Fig. 6 | DFT studies of the reaction mechanisms at the interfacial asymmetric Ni-In sites of the NiInCzr catalyst.** Free-energy diagram of CO<sub>2</sub> hydrogenation to methanol following formate pathways at Ni-In and In-In sites. The insets represent

the reverse In<sub>2</sub>O<sub>3-x</sub>/Ni interfaces and the reaction intermediates. The label (g) means gas phase. Color scheme for ball-and-stick models: blue-Ni, brown-In, gray-C, red-O, and white-H.

interface, homolytic H from Ni facilitates the reaction with a lower  $E_a$  of 1.14 eV. The reduced  $E_a$  at the Ni-In sites is attributed to the different coordination structure, where two oxygen of bi-HCOO<sup>\*</sup> species bond to Ni and In atoms, respectively, in contrast to bonding two adjacent In atoms at the In-In sites. Calculations on Ni-doped In<sub>2</sub>O<sub>3</sub>, and In<sub>2</sub>O<sub>3</sub>/Ni<sub>3</sub>InC<sub>0.5</sub> further validate the rationality of the constructed In<sub>2</sub>O<sub>3</sub> overlayer and inverse In<sub>2</sub>O<sub>3</sub>/Ni models (Supplementary Figs. 49–52). For CO formation via the COOH<sup>\*</sup> pathway, the  $E_a$  is substantially higher than the formate pathway on both models (1.55 and 1.92 eV for the In<sub>2</sub>O<sub>3</sub> and In<sub>2</sub>O<sub>3</sub>/Ni models, respectively).

Across the elementary steps, the hydrogenation of bi-HCOO<sup>\*</sup> to H<sub>2</sub>COO<sup>\*</sup> should be more kinetic relevant (Fig. 6). Interestingly, the  $E_a$  for H<sub>2</sub>COO<sup>\*</sup> formation is significantly lower on the In<sub>2</sub>O<sub>3</sub>/Ni model (1.07 eV) than on In<sub>2</sub>O<sub>3</sub> (2.26 eV), corroborating the observed acceleration of bi-HCOO<sup>\*</sup> hydrogenation at the asymmetric Ni-In sites in in-situ FTIR analysis. In addition, the energy barriers of subsequent hydrogenation of CH<sub>2</sub>O species are also lower at the Ni-In sites.

Further insights into the accelerated hydrogenation rates at asymmetric Ni-In sites were gained from electronic structure analysis, including electron density difference and electron localized function (ELF) calculations (Supplementary Fig. 53). The analysis reveals electron accumulation around the O atom of bi-HCOO<sup>\*</sup> species, accompanied by electron depletion around the C and In atoms. Importantly, the electron density between the O and C atoms at the Ni-In site is significantly reduced compared to the In-In site on In<sub>2</sub>O<sub>3</sub>. This weaker covalent bonding at the inverse In<sub>2</sub>O<sub>3-x</sub>/Ni interface facilitates faster hydrogenation of bi-HCOO<sup>\*</sup> species, consistent with the experimentally observed enhanced catalytic activity.

## Discussion

In summary, we presented a highly efficient supported Ni<sub>3</sub>InC<sub>0.5</sub> phase for CO<sub>2</sub> hydrogenation to methanol, providing a comprehensive investigation into its active sites, structure-activity relationships, and underlying reaction mechanisms. Through multiple in-situ microscopic and spectroscopic characterizations, combined with DFT calculations, we elucidated the phase transformation of NiIn alloy to

carbide and surface reconstruction mechanisms that underpin the catalytic activity of the Ni<sub>3</sub>InC<sub>0.5</sub> phase. The formation of defective In<sub>2</sub>O<sub>3-x</sub> overlayers and stable inverse In<sub>2</sub>O<sub>3-x</sub>/Ni interfaces under reaction conditions, induced by CO<sub>2</sub>-selective surface oxidation, emerged as a pivotal structural feature, enhancing CO<sub>2</sub> adsorption and stabilizing formate intermediates. These In<sub>2</sub>O<sub>3-x</sub> overlayers, in conjunction with interfacial asymmetric Ni-In sites, accelerate the hydrogenation of formate species and efficiently drive methanol production through the formate pathway. The distinctive interdependence between surface structure and reaction environment endows the Ni<sub>3</sub>InC<sub>0.5</sub> phase with exceptional stability, maintaining its structure and catalytic activity over a long-term (250 h) test without any decay. In virtue of the strong CO<sub>2</sub> activation ability of surface-oxidized Ni<sub>3</sub>InC<sub>0.5</sub>, the LDH-NiInCAL catalyst achieves an impressive 19% CO<sub>2</sub> conversion, 65% methanol selectivity, and 508.4 mg<sub>cat</sub><sup>-1</sup> h<sup>-1</sup> STY<sub>MeOH</sub> at 260 °C, 5 MPa, and 12,000 mL<sub>cat</sub><sup>-1</sup> h<sup>-1</sup>, outperforming the commercial Cu/ZnO/Al<sub>2</sub>O<sub>3</sub> catalyst and ranking among the reported state-of-the-art catalysts. This work not only deepens the fundamental understanding of surface reconstruction and active site generation in CO<sub>2</sub> hydrogenation but also highlights the immense potential of NiIn carbide-based catalysts as a robust platform for developing high-performance catalysts for industrial methanol synthesis.

## Methods

### Catalyst synthesis

The precursors were prepared using a modified ammonia carbonate co-precipitation (ACP) method<sup>66</sup>. Before synthesis, the crystalline water content of all metal nitrate hydrate materials was precisely calibrated using TGA to accurately control the molar ratio of Ni to a second metal ( $R_{Ni/M2}$ ) at 3:1 required for the stoichiometry. Unless otherwise specified, the default Ni loading amount for carbide catalysts was 33 wt.%. In a typical process, a specific amount of Ni(NO<sub>3</sub>)<sub>2</sub>·xH<sub>2</sub>O and In(NO<sub>3</sub>)<sub>3</sub>·xH<sub>2</sub>O, with a molar ratio 3:1, were dissolved in 50 mL of deionized water in a round-bottom flask. Next, 0.5 g of commercial m-ZrO<sub>2</sub> powder was dispersed into the solution with 15 min of stirring, followed by 15 min of ultrasonication. Subsequently,

15 mL of  $(\text{NH}_4)_2\text{CO}_3$  aqueous solution was added dropwise at 72 °C under vigorous stirring. After continuous stirring for 2 h and aging for another 2 h under reflux, the residue was cooled to room temperature, filtered, washed with DI water (three times, 300 mL each), and dried at 70 °C overnight. The dried cake was then ground and calcined at 350 °C for 2 h in a muffle furnace to obtain the powder oxide precursor. For the synthesis of NiInZr IMC catalyst, the obtained precursor was packed into a continuous-flow glass reactor with an inner diameter of 7 mm and reduced at 600 °C for 3 h under a flow of 30 mL  $\text{min}^{-1}$  of  $\text{H}_2$  (ramp rate, 5 °C  $\text{min}^{-1}$ ). The synthesis process for the NiInCZr carbide sample is similar, except that a flow of 30 mL  $\text{min}^{-1}$  of mixed gas (25 vol%  $\text{CO}_2/\text{H}_2$ ) was used. After cooling to room temperature, both samples were flushed with Ar for 30 min before being removed from the glass tube. Details of the preparation for other IMC and carbide samples are provided in the Supplementary Methods. The Ni loading amount and the molar quantity of ammonia carbonate are calculated using the following equations:

$$\text{Ni loading amount} = \frac{m_{\text{Ni}}}{m_{\text{ZrO}_2} + m_{\text{carbide}}} \times 100\% \quad (3)$$

$$n(\text{ammonia carbonate}) = n_{\text{Ni}} + n_{\text{In}} \times 1.5 \quad (4)$$

Where  $m$  represents the mass and  $n$  is the molar quantity.

### Catalyst characterizations

TGA for metal nitrate hydrate samples was conducted using a thermal analyzer (Q50, TA Instruments) from room temperature to 800 °C at a ramp rate of 10 °C  $\text{min}^{-1}$  in air. For in-situ carburization TGA, oxide precursors or Ni-based IMC catalysts were tested by changing the atmosphere in the thermal analyzer to 25 vol%  $\text{CO}_2/\text{H}_2$ . The samples were heated to 600 °C at a ramp rate of 5 °C  $\text{min}^{-1}$ , held for 30 min, and then allowed to cool.

XRD patterns were collected using a Rigaku MiniFlex 600 X-ray diffractometer with a Cu K $\alpha$  radiation source ( $\lambda = 1.5418 \text{ \AA}$ ). The fresh or spent catalyst powder was scanned in the  $2\theta$  range of 10–80° at a rate of 8°  $\text{min}^{-1}$  with a step size of 0.02°.

In-situ XRD was performed on the Rigaku SmartLab (8 KW) high-resolution diffractometer to study the reduction and carburization behavior of the oxide precursors under a mixed gas atmosphere (25 vol%  $\text{CO}_2/\text{H}_2$ ). To observe structural evolution during heating, the zirconia-supported NiIn precursor was scanned in the  $2\theta$  range of 15–60° at temperature intervals of 20 °C, with a rate of 15°  $\text{min}^{-1}$  and default step size under 20 mL  $\text{min}^{-1}$  of mixed gas flow until reaching 600 °C. For structural evolution during the isothermal process, the precursor was heated to 400 °C under 20 mL  $\text{min}^{-1}$  of Ar flow, which was then switched to 20 mL  $\text{min}^{-1}$  of mixed gas, and data were recorded using the same program for the following 1 h. The zirconia-supported NiZn and NiGa precursors were tested using a similar process but with the  $2\theta$  range adjusted to 30–75°.

The metal loading amount was calculated based on the X-ray fluorescence spectroscopy (XRF) results from oxide precursors using a Rigaku Supermini 200 spectrometer. The specific surface area ( $S_{\text{BET}}$ ) and pore volume were determined using the Brunauer-Emmett-Teller (BET) method and Barrett-Joyner-Halenda (BJH) desorption branch, respectively, on a Micromeritics ASAP 2460 system by  $\text{N}_2$  adsorption-desorption at 77 K. Prior to the tests, fresh catalysts were degassed at 300 °C for 12 h<sup>28</sup>.

The nanomorphology and lattice structure were observed using transmission electron microscopy (TEM) with JEM-2100 and JEM-F200 instruments. Energy-dispersive X-ray spectroscopy (EDS) elemental mapping and high-angle annular dark-field scanning transmission electron microscopy (HAADF-STEM) images were also obtained using the corresponding accessories from the TEM facilities. Aberration-corrected high-angle annular dark-field scanning transmission

electron microscopy (AC-HAADF-STEM) images were acquired on JEM-ARM200F microscope equipped with a dual-energy dispersive X-ray (EDX) spectroscopy system.

Quasi-in-situ/in-situ AC-HAADF-STEM and in-situ HRTEM experiments were conducted on JEOL ARM200F and JEM-F200 microscopes, respectively, both equipped with a Protochips Atmosphere 210 gas cell system. For in-situ experiments, the NiInZr catalyst powder was dispersed in ethanol and drop-casted onto the Protochips (Protochips Inc.) micro-electromechanical systems (MEMS) E-chips, which were subsequently assembled into a closed cell within a Protochips holder. The catalyst was firstly reduced in pure hydrogen ( $\text{H}_2$ ) with a flow rate of 0.1 sccm (~ 0.02 m/s) at 760 Torr and 600 °C (ramp rate of 1 °C/s) for 60 min and then cooled to 400 °C. Then, the sample was exposed to  $\text{CO}/\text{CO}_2/\text{H}_2$  (10:22.5:67.5) or  $\text{CO}_2/\text{H}_2$  (25:75) at 400 °C to observe structure evolution. For quasi-in-situ tests, check valves at both ends of the glass reactor were closed after synthesis. Then, the fresh NiInCZr catalyst were transferred through a glove box and Mel-Build Double tilt Atmos Defend Holder, which was then loaded into a JEOL ARM200F microscope for HAADF-STEM image taking.

In-situ Raman spectra were obtained using a HORIBA LabRAM Odyssey Deep Ultraviolet Laser Confocal Raman Spectrometer with a 532 nm laser excitation. The unsupported  $\text{Ni}_3\text{InC}_{0.5}$  powder was filled into the in-situ cell and ramped up to 400 °C with pure CO for 1 h to avoid interference from the characteristic peaks of zirconia support and passivated oxide overlayer. Afterwards, the sample was treated with 25 vol%  $\text{CO}_2/\text{H}_2$  for 2 h.

The surface chemical states of representative catalysts were determined by XPS using a Thermo Fisher K-Alpha spectrometer (Al K $\alpha$  radiation source,  $E = 1486.6 \text{ eV}$ ). For quasi-in-situ tests, check valves at both ends of the glass reactor were closed after reduction or carburization. Then, the catalysts were transferred through a glove box to the specialist vacuum sample holder of the K-Alpha facility from the glass reactor.

In-situ XPS experiments were carried out using a Thermo Fisher ESCALAB 250Xi spectrometer (Al K $\alpha$ ). Oxide Precursors were loaded and transferred into the vacuum chamber. After recording the initial states,  $\text{H}_2$  was introduced into the system to reduce the samples at 400 °C for 2 h, followed by cooling to room temperature and vacuuming the system for data acquisition. Subsequently, the feed was switched to mixed gas (25 vol%  $\text{CO}_2/\text{H}_2$ ) to carburize the reduced IMCs at 400 °C for 2 h before final scanning. All spectra were calibrated to the adventitious carbon C 1s peak at 284.8 eV and further analyzed using the Advantage software.

Although XAS by transmission mode shows more bulk information of the samples, by in-situ experiment and suitable sample comparison, it can still be used to probe the changes on the surface. In-situ XAS measurements on Ni K-edge were conducted in transmission mode using wafer-like samples (I.D. 10 mm pellets) in a customized reaction cell at the X-ray absorption fine structure for catalysis (XAFCA) beamline of the Singapore Synchrotron Light Source (SSLS). Specifically, the NiInZrO precursor sample was sequentially treated with  $\text{H}_2$ , 25 vol%  $\text{CO}_2/\text{H}_2$ ,  $\text{CO}/\text{H}_2$ , and then again 25 vol.%  $\text{CO}_2/\text{H}_2$  at a constant temperature of 400 °C, with each gas atmosphere maintained for 1 h. Ni K-edge XAS spectra were collected throughout the process. Quasi-in-situ XAS on the Ni K-edge was measured under the transmission mode at Synchrotron Light Research Institute (Beamline 1.1W Multiple X-ray Techniques) in Thailand. Like quasi-in-situ XPS tests, the activated catalysts were transferred into a glove box to minimize oxidation. An appropriate amount of sample was spread evenly in a plastic frame and sealed with Kapton tape<sup>44</sup>. The XAS data were processed using Demeter software packages<sup>67</sup>.

Temperature-programmed experiments were performed using a Micromeritics AutoChem II 2920 TPR/TPD instrument equipped with a Hiden QIC-20 mass spectrometer (MS).  $\text{H}_2$ -temperature programmed

reduction ( $\text{H}_2$ -TPR) was used to analyze the reducibility of the oxide precursors. Approximately 100 mg of the precursor was pretreated in an Ar flow ( $30 \text{ mL min}^{-1}$ ) at  $200^\circ\text{C}$  for 1 h, then cooled to  $60^\circ\text{C}$  to remove the moisture and other contaminants. The sample was then reduced under a flow of 10 vol%  $\text{H}_2/\text{Ar}$  ( $30 \text{ mL min}^{-1}$ ) and heated to  $800^\circ\text{C}$  with a ramp rate of  $10^\circ\text{C min}^{-1}$ . A cooling trap was installed between the sample and the thermal conductivity detector (TCD) to remove the water formed during the reduction.

The same instrument was used for TPD of  $\text{H}_2$ ,  $\text{CO}_2$ , and  $\text{CO}$ . Approximately 100 mg of the sample was treated at  $400^\circ\text{C}$  for 1 h by  $30 \text{ mL min}^{-1}$  of pre-treatment gas ( $\text{H}_2$  for IMC catalysts or mixed gas for carbide catalysts), followed by flushing with He ( $30 \text{ mL min}^{-1}$ ) for 30 min to clean its surface. After cooling to  $60^\circ\text{C}$ , the sample was exposed to  $\text{H}_2$  flow ( $30 \text{ mL min}^{-1}$ ) for 30 min for saturate adsorption of  $\text{H}_2$ , then purged with carrier gas, Ar ( $30 \text{ mL min}^{-1}$ ), for 30 min. Once the TCD signal baseline stabilized, the sample was heated to  $800^\circ\text{C}$  at a rate of  $10^\circ\text{C min}^{-1}$ , recording the TPD profile from TCD. For the TPD of  $\text{CO}_2$  and  $\text{CO}$ , the sample was treated similarly, except that  $\text{CO}_2$  or  $\text{CO}$  replaced  $\text{H}_2$  to saturate the surface, and carrier gas was changed to He ( $30 \text{ mL min}^{-1}$ ). The MS signals of  $\text{H}_2$ ,  $\text{H}_2\text{O}$ ,  $\text{CO}$ , and  $\text{CO}_2$  ( $m/z = 2, 18, 28$ , and  $44$ , respectively) were recorded simultaneously as the sample was heated to record the TPD profile.

$\text{H}_2$ -TPR coupled with MS was employed to analyze the surface  $\text{In}_2\text{O}_3$  species on both fresh and spent catalysts. After synthesis or catalytic evaluation, approximately 0.1 g of the sample was cooled to  $60^\circ\text{C}$  under an Ar flow, with the reactor effluent connected to a Shimadzu GCMS-QP2020 NX instrument. Subsequently, the sample was subjected to reduction under a 10 vol%  $\text{H}_2/\text{Ar}$  ( $30 \text{ mL min}^{-1}$ ) while being heated to  $700^\circ\text{C}$  at a ramp rate of  $10^\circ\text{C min}^{-1}$ . The actual temperature of the fixed bed was monitored using a thermocouple.

The adsorption, formation, and consumption of the intermediates during the reaction were monitored by in-situ Fourier transform infrared spectroscopy (in-situ FTIR) in transmission mode using a Thermo Fisher Nicolet iS50 spectrometer equipped with a Specac high-temperature high-pressure (HTHP) cell and an MCT/A detector. Each spectrum was recorded at  $4 \text{ cm}^{-1}$  resolutions with 32 scans. To reduce the strong infrared light adsorption by Ni-base IMC and carbide catalysts, 5 mg of the sample was diluted with 30 mg  $\text{CaF}_2$ , ground, and pressed into a 12 mm diameter wafer. The wafer was activated with  $30 \text{ mL min}^{-1}$  of 25 vol%  $\text{CO}_2/\text{H}_2$  at  $400^\circ\text{C}$  for 1 h, purged with Ar ( $30 \text{ mL min}^{-1}$ ) for 30 min to remove the adsorbates, and then cooled to the target temperature for background spectra collection. For the  $\text{CO}_2$  adsorption and hydrogenation process, the sample was exposed to  $\text{CO}_2$  ( $30 \text{ mL min}^{-1}$ ) at  $280^\circ\text{C}$  and ambient pressure until the spectra stabilized. The system was then pressurized to 2 MPa with  $\text{CO}_2$ , followed by switching the feed to  $\text{H}_2$  to monitor changes in the adsorbed  $\text{CO}_2$  species for 60 min. For the  $\text{CO}_2$  hydrogenation process,  $30 \text{ mL min}^{-1}$  of mixed gas ( $\text{H}_2: \text{CO}_2 = 3/1$ ) was used to activate the catalyst. After cooling to  $280^\circ\text{C}$  under Ar flow, the activated sample was exposed to a mixed gas ( $\text{H}_2: \text{CO}_2 = 3/1$ ,  $30 \text{ mL min}^{-1}$ ) at ambient pressure until the spectra stabilized, then pressurized to 2 MPa.

The influence of temperature on intermediates was studied by monitoring the reaction at different temperatures ( $220/260/280$ , and  $300^\circ\text{C}$ ). After mixed gas activation, the cell was cooled to  $100^\circ\text{C}$ , and the mixed gas ( $\text{H}_2: \text{CO}_2 = 3/1$ ) was introduced at  $30 \text{ mL min}^{-1}$  to pressurize to 0.3 MPa. After equilibrium, the sample was heated to  $140^\circ\text{C}$ ,  $180^\circ\text{C}$ ,  $220^\circ\text{C}$ ,  $260^\circ\text{C}$ ,  $280^\circ\text{C}$ , and  $300^\circ\text{C}$  at a rate of  $10^\circ\text{C min}^{-1}$ , with steady spectra collected at each temperature.

To study the consumption speed of intermediates during hydrogenation, after saturating the sample's surface at  $280^\circ\text{C}$  and 2 MPa under mixed gas flow ( $\text{H}_2: \text{CO}_2 = 3/1$ ,  $30 \text{ mL min}^{-1}$ ), the sample was purged by  $30 \text{ mL min}^{-1}$  of  $\text{H}_2$  for 150 min. FTIR spectra were collected every 10 s during all processes.

## Catalyst evaluation

$\text{CO}_2$  hydrogenation was conducted in a fixed-bed continuous-flow stainless steel reactor. Before the evaluation, the prepared catalysts were pressed, crushed, and sieved into 40–60 mesh granules to minimize the impact of internal diffusion. Approximately 0.1 g of the sieved catalyst granules was loaded into a reactor tube with an external diameter of 3/8 inch and a thickness of 1 mm. To remove the passivated layer on the nanoparticle surface, Ni-based IMC catalysts were activated using  $30 \text{ mL min}^{-1}$  of  $\text{H}_2$  at  $400^\circ\text{C}$  for 1 h under ambient pressure. For the Ni-based carbide catalysts,  $30 \text{ mL min}^{-1}$  of mixed gas ( $\text{H}_2/\text{CO}_2 = 3/1$ ) was used for pretreatment instead. For general catalyst evaluation, after cooling to the target reaction temperature, the reactor was pressurized to 4 MPa with mixed gas ( $\text{H}_2:\text{CO}_2:\text{N}_2 = 72/24/4$ , with  $\text{N}_2$  as an internal standard). To prevent condensation of the products,  $\text{H}_2\text{O}$  and  $\text{CH}_3\text{OH}$ , the gas line between the reactor and the online gas chromatography (GC, Shimadzu GC-2014C) was maintained at  $150^\circ\text{C}$ . The gas products were directly analyzed by the online GC, equipped with two loops: one connected to two packed columns, porapak N ( $1 \text{ m} \times 3 \text{ mm}$ ) and TDX-01 ( $3 \text{ m} \times 3 \text{ mm}$ ), with a TCD, and the second connected to a capillary column, SH-Q-BOND ( $30 \text{ m} \times 0.32 \text{ mm}$ ), with a flame ionization detector (FID). The calculations of catalytic activity, including  $\text{CO}_2$  conversion ( $X_{\text{CO}_2}$ ), methanol selectivity ( $S_{\text{MeOH}}$ ), and methanol space-time yield ( $STY_{\text{MeOH}}$ ), are detailed in the Supplementary Information, along with the procedure for the reaction kinetics study.

## Computational details

Spin-polarized DFT calculations were performed using the Vienna Ab initio Simulation Package (VASP, version 5.4.1), with the generalized gradient approximation (GGA) of Perdew-Burke-Ernzerhof (PBE) to describe electron exchange and correlation<sup>68,69</sup>. The cut-off energy of the plane-wave basis set was set to  $400 \text{ eV}$ <sup>70</sup>. The convergence tolerances for the energy optimization criterion were set to  $10^{-5} \text{ eV}$ , and the atomic forces in the optimized structures were smaller than  $0.03 \text{ eV \AA}^{-1}$ .

We chose the c- $\text{In}_2\text{O}_3$  (100) surface termination as it is the most stable surface under  $\text{CO}_2$  hydrogenation reaction conditions<sup>71</sup>. Meanwhile, according to our AC-STEM observation, the exposed facet of the surface c- $\text{In}_2\text{O}_3$  layer on  $\text{Ni}_3\text{InC}_{0.5}$  NPs is (100) plane. A  $3 \times 3$ -unit cell was used to construct a c- $\text{In}_2\text{O}_3$  (100) slab model consisting of 24 In atoms and 32 O atoms distributed in three In-O-In layers. The atoms in the bottom layer were frozen, while the top two In-O-In layers were relaxed. The Brillouin zone was sampled using a  $3 \times 3 \times 1$   $k$ -point grid based on the Monkhorst-Pack method. Considering the surface oxidation mechanism of  $\text{Ni}_3\text{InC}_{0.5}$  under reaction conditions and the core-shell structure of the  $\text{Ni}_3\text{InC}_{0.5}\text{-In}_2\text{O}_3$ , when metallic In atoms are oxidized, Ni atoms are left and fixed between the bulk  $\text{Ni}_3\text{InC}_{0.5}$  and surface  $\text{In}_2\text{O}_3$  layer. Thus, the model of Ni (111)-supported  $\text{In}_2\text{O}_3$  clusters was constructed to represent the interface structure. The bottom two layers of Ni atoms were frozen, while one layer of Ni and supported  $(\text{In}_2\text{O}_3)_2$  clusters were allowed to perturb. A  $1 \times 1 \times 1$   $k$ -point grid generated with the Monkhorst-Pack scheme was found to give converged results. More detailed theoretical calculations were provided in Supplementary Information.

## Data availability

All data needed to draw the conclusions of this study are presented in the paper and/or the Supplementary Information file. Source data is provided with this paper. All data are available from the corresponding author upon request. Source data are provided with this paper.

## References

1. Tao, F. & Salmeron, M. Surface restructuring and predictive design of heterogeneous catalysts. *Science* **386**, eadq0102 (2024).

- Zhang, X. et al. Reversible loss of core–shell structure for Ni–Au bimetallic nanoparticles during CO<sub>2</sub> hydrogenation. *Nat. Catal.* **3**, 411–417 (2020).
- Dong, Z. et al. Revealing synergetic structural activation of a CuAu surface during water–gas shift reaction. *Proc. Natl. Acad. Sci. USA* **119**, e2120088119 (2022).
- Liu, X. et al. Atomically thick oxide overcoating stimulates low-temperature reactive metal–support interactions for enhanced catalysis. *J. Am. Chem. Soc.* **145**, 6702–6709 (2023).
- Wang, J. et al. Confinement-induced indium oxide nanolayers formed on oxide support for enhanced CO<sub>2</sub> hydrogenation reaction. *J. Am. Chem. Soc.* **146**, 5523–5531 (2024).
- Wu, C. H. et al. Bimetallic synergy in cobalt–palladium nanocatalysts for CO oxidation. *Nat. Catal.* **2**, 78–85 (2018).
- Ding, X., Zhu, M., Sun, B., Yang, Z. & Han, Y.-F. An overview on dynamic phase transformation and surface reconstruction of iron catalysts for catalytic hydrogenation of CO<sub>x</sub> for hydrocarbons. *ACS Catal.* **14**, 6137–6168 (2024).
- Cai, L. et al. Formation of a porous crystalline Mg<sub>1-x</sub>Al<sub>2</sub>O<sub>y</sub> overlayer on metal catalysts via controlled solid-state reactions for high-temperature stable catalysis. *Angew. Chem. Int. Ed.* **63**, e202404398 (2024).
- Sandoval-Diaz, L. et al. Metastable nickel–oxygen species modulate rate oscillations during dry reforming of methane. *Nat. Catal.* **7**, 161–171 (2024).
- Kim, K. Y. et al. Layered double hydroxide-derived intermetallic Ni<sub>3</sub>GaC<sub>0.25</sub> catalysts for dry reforming of methane. *ACS Catal.* **11**, 11091–11102 (2021).
- Zhao, H. et al. Atomic-scale structure dynamics of nanocrystals revealed by in situ and environmental transmission electron microscopy. *Adv. Mater.* **35**, 2206911 (2023).
- Chen, L. et al. Advances in in situ/operando techniques for catalysis research: enhancing insights and discoveries. *Surf. Sci. Technol.* **2**, 9 (2024).
- Zhong, J. et al. State of the art and perspectives in heterogeneous catalysis of CO<sub>2</sub> hydrogenation to methanol. *Chem. Soc. Rev.* **49**, 1385–1413 (2020).
- Zabilskiy, M. et al. The unique interplay between copper and zinc during catalytic carbon dioxide hydrogenation to methanol. *Nat. Commun.* **11**, 2409 (2020).
- Amann, P. et al. The state of zinc in methanol synthesis over a Zn/ZnO/Cu(211) model catalyst. *Science* **376**, 603–608 (2022).
- Liang, B. et al. Investigation on deactivation of Cu/ZnO/Al<sub>2</sub>O<sub>3</sub> catalyst for CO<sub>2</sub> hydrogenation to methanol. *Ind. Eng. Chem. Res.* **58**, 9030–9037 (2019).
- Ye, J., Liu, C. & Ge, Q. DFT study of CO<sub>2</sub> adsorption and hydrogenation on the In<sub>2</sub>O<sub>3</sub> surface. *J. Phys. Chem. C* **116**, 7817–7825 (2012).
- Ye, J., Liu, C., Mei, D. & Ge, Q. Active oxygen vacancy site for methanol synthesis from CO<sub>2</sub> hydrogenation on In<sub>2</sub>O<sub>3</sub>(110): a DFT study. *ACS Catal.* **3**, 1296–1306 (2013).
- Rui, N. et al. CO<sub>2</sub> hydrogenation to methanol over Pd/In<sub>2</sub>O<sub>3</sub>: effects of Pd and oxygen vacancy. *Appl. Catal. B Environ.* **218**, 488–497 (2017).
- Frei, M. S. et al. Nanostructure of nickel-promoted indium oxide catalysts drives selectivity in CO<sub>2</sub> hydrogenation. *Nat. Commun.* **12**, 1960 (2021).
- Frei, M. S., et al. Atomic-scale engineering of indium oxide promotion by palladium for methanol production via CO<sub>2</sub> hydrogenation. *Nat. Commun.* **10**, 3377 (2019).
- Frei, M. S. et al. Role of zirconia in indium oxide-catalyzed CO<sub>2</sub> hydrogenation to methanol. *ACS Catal.* **10**, 1133–1145 (2020).
- Yang, C. et al. Strong electronic oxide–support interaction over In<sub>2</sub>O<sub>3</sub>/ZrO<sub>2</sub> for highly selective CO<sub>2</sub> hydrogenation to methanol. *J. Am. Chem. Soc.* **142**, 19523–19531 (2020).
- Alamer, A. M. et al. Design of dilute palladium–indium alloy catalysts for the selective hydrogenation of CO<sub>2</sub> to methanol. *ACS Catal.* **13**, 9987–9996 (2023).
- Li, M. M. et al. Methanol synthesis at a wide range of H<sub>2</sub>/CO<sub>2</sub> ratios over a Rh–In bimetallic catalyst. *Angew. Chem. Int. Ed.* **59**, 16039–16046 (2020).
- Shen, C. et al. Highly active Ir/In<sub>2</sub>O<sub>3</sub> catalysts for selective hydrogenation of CO<sub>2</sub> to methanol: experimental and theoretical studies. *ACS Catal.* **11**, 4036–4046 (2021).
- Sun, Q. et al. Breaking the conversion–selectivity trade-off in methanol synthesis from CO<sub>2</sub> using dual intimate oxide/metal interfaces. *J. Am. Chem. Soc.* **146**, 28885–28894 (2024).
- Meng, C., et al. Oxygen-deficient metal oxides supported nano-intermetallic InNi<sub>3</sub>C<sub>0.5</sub> toward efficient CO<sub>2</sub> hydrogenation to methanol. *Sci. Adv.* **7**, eabi6012 (2021).
- Belova, I. V. & Murch, G. E. Percolation and the anti-structural bridge mechanism for diffusion in ordered alloys of the L1<sub>2</sub> type. *Intermetallics* **6**, 403–411 (1998).
- Semenova, O., Krachler, R. & Ipser, H. Estimation of point defect formation energies in the DO<sub>19</sub>-type intermetallic compound Ti<sub>3</sub>Al. *Solid State Sci.* **4**, 1113–1117 (2002).
- Aparna, C., Shetty, P. K., Mahesha, M. G., Yashodhara, I. & Karunakara, N. Sensitivity estimation of indium oxide thin film for gamma sensing. *J. Mater. Sci.* **58**, 11374–11391 (2023).
- Wiranwetchayan, O. et al. Effect of nanoporous In<sub>2</sub>O<sub>3</sub> film fabricated on TiO<sub>2</sub>–In<sub>2</sub>O<sub>3</sub> photoanode for photovoltaic performance via a sparking method. *J. Solid State Electrochem.* **22**, 2531–2543 (2018).
- Gan, J. et al. Oxygen vacancies promoting photoelectrochemical performance of In<sub>2</sub>O<sub>3</sub> nanocubes. *Sci. Rep.* **3**, 1–7 (2013).
- Mironova-Ulmane, N. et al. Raman scattering in nanosized nickel oxide NiO. *J. Phys. Conf. Ser.* **93**, 012039 (2007).
- Cheng, M., Fan, H., Song, Y., Cui, Y. & Wang, R. Interconnected hierarchical NiCo<sub>2</sub>O<sub>4</sub> microspheres as high-performance electrode materials for supercapacitors. *Dalton Trans.* **46**, 9201–9209 (2017).
- Zhu, J., et al. Dynamic structural evolution of iron catalysts involving competitive oxidation and carburization during CO<sub>2</sub> hydrogenation. *Sci. Adv.* **8**, eabm3629 (2022).
- Ding, Y. et al. Revealing the effect of metal–support interactions at the Ni/In<sub>2</sub>O<sub>3</sub>(111) interface on the selective CO<sub>2</sub> hydrogenation. *Appl. Catal. B Environ.* **343**, 123508 (2024).
- Chen, T. et al. Unraveling highly tunable selectivity in CO<sub>2</sub> hydrogenation over bimetallic In–Zr oxide catalysts. *ACS Catal.* **9**, 8785–8797 (2019).
- Xu, M. et al. Renaissance of strong metal–support interactions. *J. Am. Chem. Soc.* **146**, 2290–2307 (2024).
- Leybo, D. et al. Metal–support interactions in metal oxide-supported atomic, cluster, and nanoparticle catalysis. *Chem. Soc. Rev.* **53**, 10450–10490 (2024).
- Durussel, P. H., Burri, G. & Feschotte, P. The binary system Ni–In. *J. Alloy. Compd.* **257**, 253–258 (1997).
- Ge, X. et al. Enhanced acetylene semi-hydrogenation on a subsurface carbon tailored Ni–Ga intermetallic catalyst. *J. Mater. Chem. A* **10**, 19722–19731 (2022).
- Ge, X. et al. Mechanism driven design of trimer Ni<sub>3</sub>Sb<sub>2</sub> site delivering superior hydrogenation selectivity to ethylene. *Nat. Commun.* **13**, 5534 (2022).
- Hongmanorom, P., Ashok, J., Chirawatkul, P. & Kawi, S. Interfacial synergistic catalysis over Ni nanoparticles encapsulated in mesoporous ceria for CO<sub>2</sub> methanation. *Appl. Catal. B Environ.* **297**, 120454 (2021).

45. Saeidi, S. et al. Recent advances in CO<sub>2</sub> hydrogenation to value-added products — Current challenges and future directions. *Prog. Energy Combust. Sci.* **85**, 100905 (2021).
46. Lin, S. et al. Ni–Zn dual sites switch the CO<sub>2</sub> hydrogenation selectivity via tuning of the d-band center. *ACS Catal.* **12**, 3346–3356 (2022).
47. Tsoukalou, A. et al. Structural evolution and dynamics of an In<sub>2</sub>O<sub>3</sub> catalyst for CO<sub>2</sub> hydrogenation to methanol: an operando XAS-XRD and in situ TEM study. *J. Am. Chem. Soc.* **141**, 13497–13505 (2019).
48. Cai, Y. et al. Antiover-reduction of Ni/In<sub>2</sub>O<sub>3</sub> nanocatalysts by atomic layer deposition of Al<sub>2</sub>O<sub>3</sub> films for durable CO<sub>2</sub> hydrogenation to methanol. *ACS Catal.* **14**, 8463–8479 (2024).
49. He, Y. et al. Significant roles of surface hydrides in enhancing the performance of Cu/BaTiO<sub>2.8</sub>H<sub>0.2</sub> catalyst for CO<sub>2</sub> hydrogenation to methanol. *Angew. Chem. Int. Ed.* **63**, e202313389 (2024).
50. Rothenberg, G. *Catalysis: Concepts and Green Applications*. (Wiley-VCH, 2008).
51. Wang, Y. et al. Unraveling the role of basic sites in the hydrogenation of CO<sub>2</sub> to formic acid over Ni-based catalysts. *J. Catal.* **430**, 115357 (2024).
52. Zhang, H., Mao, D., Zhang, J. & Wu, D. Regulating the crystal structure of layered double hydroxide-derived Co–In catalysts for highly selective CO<sub>2</sub> hydrogenation to methanol. *Chem. Eng. J.* **452**, 139144 (2023).
53. Dewangan, N. et al. Recent progress on layered double hydroxide (LDH) derived metal-based catalysts for CO<sub>2</sub> conversion to valuable chemicals. *Catal. Today* **356**, 490–513 (2020).
54. Huang, Z. et al. CO<sub>2</sub> hydrogenation over mesoporous Ni–Pt/SiO<sub>2</sub> nanorod catalysts: Determining CH<sub>4</sub>/CO selectivity by surface ratio of Ni/Pt. *Chem. Eng. Sci.* **247**, 117106 (2022).
55. Fehr, S. M., Nguyen, K. & Krossing, I. Realistic operando-DRIFTS studies on Cu/ZnO catalysts for CO<sub>2</sub> hydrogenation to methanol – direct observation of mono-ionized defect sites and implications for reaction intermediates. *ChemCatChem* **14**, e202101500 (2022).
56. Tsoukalou, A. et al. Surface intermediates in In-based ZrO<sub>2</sub>-supported catalysts for hydrogenation of CO<sub>2</sub> to methanol. *J. Phys. Chem. C.* **126**, 1793–1799 (2022).
57. Feng, Z. et al. Asymmetric sites on the ZnZrO<sub>x</sub> catalyst for promoting formate formation and transformation in CO<sub>2</sub> hydrogenation. *J. Am. Chem. Soc.* **145**, 12663–12672 (2023).
58. Fehr, S. M. & Krossing, I. Spectroscopic signatures of pressurized carbon dioxide in diffuse reflectance infrared spectroscopy of heterogeneous catalysts. *ChemCatChem* **12**, 2622–2629 (2020).
59. Jin, S. et al. Atom-by-atom design of Cu/ZrO<sub>x</sub> clusters on MgO for CO<sub>2</sub> hydrogenation using liquid-phase atomic layer deposition. *Nat. Catal.* **7**, 1199–1212 (2024).
60. Wang, Q. et al. Effect of interstitial carbon atoms in core-shell Ni<sub>3</sub>ZnCo<sub>0.7</sub>/Al<sub>2</sub>O<sub>3</sub> catalyst for high-performance dry reforming of methane. *Appl. Catal. B Environ.* **317**, 121806 (2022).
61. Regalado Vera, C. Y. et al. Mechanistic understanding of support effect on the activity and selectivity of indium oxide catalysts for CO<sub>2</sub> hydrogenation. *Chem. Eng. J.* **426**, 131767 (2021).
62. Liu, L., Mezari, B., Kosinov, N. & Hensen, E. J. M. Al promotion of In<sub>2</sub>O<sub>3</sub> for CO<sub>2</sub> hydrogenation to methanol. *ACS Catal.* **13**, 15730–15745 (2023).
63. Wu, C. et al. Inverse ZrO<sub>2</sub>/Cu as a highly efficient methanol synthesis catalyst from CO<sub>2</sub> hydrogenation. *Nat. Commun.* **11**, 5767 (2020).
64. Yang, M., et al. Unlocking a dual-channel pathway in CO<sub>2</sub> hydrogenation to methanol over single-site zirconium on amorphous silica. *Angew. Chem. Int. Ed.* **63**, e202312292 (2024).
65. Lozano-Reis, P., Prats, H., Gamallo, P., Illas, F. & Sayós, R. Multiscale study of the mechanism of catalytic CO<sub>2</sub> hydrogenation: Role of the Ni(111) facets. *ACS Catal.* **10**, 8077–8089 (2020).
66. Wei, Y. et al. Catalytic roles of In<sub>2</sub>O<sub>3</sub> in ZrO<sub>2</sub>-based binary oxides for CO<sub>2</sub> hydrogenation to methanol. *Mol. Catal.* **525**, 112354 (2022).
67. Ravel, B. & Newville, M. ATHENA, ARTEMIS, HEPHAESTUS: data analysis for X-ray absorption spectroscopy using IFEFFIT. *J. Synchrotron Radiat.* **12**, 537–541 (2005).
68. Perdew, J. P., Burke, K. & Wang, Y. Generalized gradient approximation for the exchange-correlation hole of a many-electron system. *Phys. Rev. B* **54**, 16533–16539 (1996).
69. Kresse, G. & Furthmüller, J. Efficient iterative schemes for ab initio total-energy calculations using a plane-wave basis set. *Phys. Rev. B* **54**, 11169–11186 (1996).
70. Hu, J. et al. Sulfur vacancy-rich MoS<sub>2</sub> as a catalyst for the hydrogenation of CO<sub>2</sub> to methanol. *Nat. Catal.* **4**, 242–250 (2021).
71. Zhang, M., Wang, W. & Chen, Y. Insight of DFT and ab initio atomistic thermodynamics on the surface stability and morphology of In<sub>2</sub>O<sub>3</sub>. *Appl. Surf. Sci.* **434**, 1344–1352 (2018).

## Acknowledgements

This work was completed at Key Laboratory for Green Chemical Technology of Ministry of Education, Collaborative Innovation Center of Chemical Science and Engineering, School of Chemical engineering and technology, Tianjin University, and Department of Chemical and Biomolecular Engineering, College of Design and Engineering, National University of Singapore, in collaboration with Department of Materials Science and Engineering, College of Design and Engineering, National University of Singapore, Singapore Synchrotron Light Source, and Institute of Sustainability for Chemicals, Energy and Environment, Agency for Science, Technology and Research, Singapore. This project was supported by the National Natural Science Foundation of China (22178265, 22378310, 22438010), National Key Research and Development Program of China (2024YFB4105303) and the National Research Foundation, Singapore, and A\*STAR under its Low-Carbon Energy Research (LCER) Funding Initiative (FI) Project (U2102d2011, WBS: A-8000278-00-00, and LCERFI01-0033 | U2102d2006). We also thank Dr. Tongtong Gao, Dr. Hui Fang, Dr. Donghui Wang, and Dr. Nana Tian from Analytical Test Center of Tianjin University for assistance in in-situ XRD, XPS, Raman, and FTIR tests.

## Author contributions

J.C., M.L., S.K., and X.M. conceived the project. Yo. W., M.L., S.K., and X.M. supervised the project and revised the manuscript. J.C. conducted most experiments, analyzed data, and drafted the initial manuscript. T.X. performed the theoretical calculations, prepared the DFT draft, and revised the manuscript. B. Y. and Q.H. carried out in-situ AC-HAADF-STEM tests. H.Z. participated in catalyst synthesis, evaluations, and in-situ FTIR tests. M.T. assisted in analyzing the characterizations and provided suggestions for further studies. S.X. carried out in-situ XAS experiments and assisted with XAS data analysis. S.T. and W.J. performed in-situ Raman tests. Q.Y. conducted some of the TEM measurements. Z.H. and Z.Z. assisted with in-situ TEM. K.H.L., Yu.W., and J.L. helped to revise the manuscript. X.H. and X.Z. helped to conduct and analyze chemisorption experiments. All authors discussed the results and commented on the manuscript.

## Competing interests

The authors declare no competing interests.

## Additional information

**Supplementary information** The online version contains supplementary material available at <https://doi.org/10.1038/s41467-025-65929-z>.

**Correspondence** and requests for materials should be addressed to Maoshuai Li, Yong Wang, Sibudjing Kawi or Xinbin Ma.

**Peer review information** *Nature Communications* thanks the anonymous reviewers for their contribution to the peer review of this work. A peer review file is available.

**Reprints and permissions information** is available at <http://www.nature.com/reprints>

**Publisher's note** Springer Nature remains neutral with regard to jurisdictional claims in published maps and institutional affiliations.

**Open Access** This article is licensed under a Creative Commons Attribution-NonCommercial-NoDerivatives 4.0 International License, which permits any non-commercial use, sharing, distribution and reproduction in any medium or format, as long as you give appropriate credit to the original author(s) and the source, provide a link to the Creative Commons licence, and indicate if you modified the licensed material. You do not have permission under this licence to share adapted material derived from this article or parts of it. The images or other third party material in this article are included in the article's Creative Commons licence, unless indicated otherwise in a credit line to the material. If material is not included in the article's Creative Commons licence and your intended use is not permitted by statutory regulation or exceeds the permitted use, you will need to obtain permission directly from the copyright holder. To view a copy of this licence, visit <http://creativecommons.org/licenses/by-nc-nd/4.0/>.

© The Author(s) 2025